

Three-Body Cluster Structure of $\Lambda^7\text{Li}$ Hypernucleus

Theingi¹, Khin Swe Myint²
Associate Professor¹, Emeritus Professor²
Physics Department^{1,2}

Mandalay University of Distance Education¹, Mandalay University²
theingimandalar@gmail.com¹, profkhinswemyint@gmail.com²

Abstract

In order to study the structure change in core nucleus ${}^6\text{Li}$ by addition of Λ particle, we have performed $\Lambda^7\text{Li}$ within the frame work of three-body α - Λ calculation by using Kamimura's coupled-rearrangement channel method. The bound states and resonance states of subsystems in $\Lambda^7\text{Li}$ have been analyzed with correct boundary condition by applying the Complex Rotation Method (CRM). Pauli forbidden states between α and d clusters were excluded from the solution of Schrödinger equation by implementing the Orthogonality Condition Model (OCM). Our calculated Λ -binding energy is in good agreement with the experimental value, 5.58 ± 0.03 MeV. It is discovered that Λ -binding energy is larger than the separation energy of core nucleus ${}^6\text{Li}$ (α - d), 1.48 MeV. Root mean square distance of α - d in $\Lambda^7\text{Li}$ was found to be 3.44 fm which is significantly smaller than that of α - d in free space, 4.1 fm. From this research work, it is found that inclusion of Λ particle gives more binding to the core nucleus.

Keywords- Coupled- rearrangement channel method, Complex Rotation Method, Pauli forbidden states, shrinkage effect

1. Introduction

The alpha cluster model [1] is based on the assumption that the alpha particle is taken as a single structure less entity. This assumption of the alpha cluster model is the fact that the alpha is tightly bound with an unusual stable structure. Thus the alpha particle is treated as rigid entity without internal structure. The cluster picture of the nuclei is justified when the internal binding energy of each cluster is larger than the relative binding energy between the clusters.

2. Aim

The studying of the structure of hypernuclear systems, we expect, would reveal some knowledge about effective hyperon-nucleon and hyperon-nucleus interactions in nuclear medium. Our interests are in how hyperon embedded in the nucleus behaves, how the nucleus responds to the participation of the hyperon and

ultimately what emerge as new and genuine hypernuclear phenomena.

3. Interactions

To solve the Λ bound states in ${}^6\text{Li}$ (α - d) system, it is necessary to know the α - d , Λ - α and Λ - d interactions.

3.1. α - d Potential

We have used the α - d potential that introduced by Furutani et al., [2]. It has been often used in the Orthogonality Condition Model (OCM) based cluster-model study of light nuclei. It reproduces reasonably well the low-lying state and low-energy scattering phase shifts of the α - d system. The potential are described in the following parity dependent form with the central and spin-orbit terms.

$$V_{\alpha-d}(r) = -74.42 e^{-\left(\frac{r}{2.236}\right)^2} - 8.0 e^{-\left(\frac{r}{1.826}\right)^2} \vec{l} \cdot \vec{s}_d \quad \text{for all } l. \quad (1)$$

where l is the relative angular momentum between α and d , and \vec{s}_d is the spin of deuteron. The relative angular momenta, l between alpha and deuteron are 0 for ground state and 2 for $3^+, 2^+, 1^+$ excited states. Since the spin of deuteron (\vec{s}_d) is 1, the angular momenta and parity for α - d system are 1^+ for ground state and $3^+, 2^+, 1^+$ for three excited states. The forbidden states between alpha and deuteron are 0s and 0p.

We also employed Nishioka [3] α - d potential in $\Lambda^7\text{Li}$ calculation as follows;

$$V_{\alpha-d}(r) = -72.594 e^{-\left(\frac{r}{2.294}\right)^2}. \quad (2)$$

3.2. Λ - α Potential

Among the various Λ - α potentials, we first discuss the potential which is introduced by Myint, Shinmura and Akaishi [4], which we call it MSA Λ - α potential. It is derived from the realistic one-boson-exchange YN potential of Nijimegen model D [5]. The original Nijimegen potential is simulated by Shinmura so as to reproduce the phase shift parameters as the original Nijimegen potential. The effective Λ - N potential is derived by the Bruckner Theory. The required Λ - N

potential which based on this effective Λ -N potential is constructed by Hartree-Fock method.

$$V_{\Lambda-\alpha}(r) = 91.0e^{-\left(\frac{r}{1.3}\right)^2} - 95.0e^{-\left(\frac{r}{1.7}\right)^2} \quad (3)$$

Our calculated binding energy and r.m.s distance are 3.12 MeV and 3.11 fm respectively.

Kurihara [6] Λ - α central repulsion is expected to have significant effects on the structure of light hypernuclei like Λ 7Li and $\Lambda\Lambda$ 6He system. From their investigation, the realistic Λ - α potential must have a central repulsion and this feature is a direct appearance of the repulsive core effect of the Λ -N interaction.

Kurihara Λ - α two-range Gaussian form is

$$V_{\Lambda-\alpha}(r) = 450.4e^{-\left(\frac{r}{1.25}\right)^2} - 404.9e^{-\left(\frac{r}{1.41}\right)^2} \quad (4)$$

3.3. Lambda-Deuteron Potential

We constructed the phenomenological Λ -d potential by adjusting the parameters to fit the value $B_\Lambda=0.13\pm0.05$ MeV [7]. This potential is three-range Gaussian form as follows:

$$V_{\Lambda-d}(r) = -30.84e^{-\left(\frac{r}{1.78}\right)^2} - 103.4e^{-\left(\frac{r}{1.32}\right)^2} + 181.7e^{-\left(\frac{r}{1.08}\right)^2}. \quad (5)$$

4. Complex Coordinate Rotation Method

We use the method of complex coordinate rotation to investigate the bound state and resonance states of α -d. According to the complex rotation method [8], the following transformation

$$r \rightarrow r e^{i\theta}$$

is carried out, where θ is a real number called rotation angle. Under this transformation, wave function is defined as

$$\Psi(r) \rightarrow \Psi(re^{i\theta}) = \Psi_\theta(r) = \hat{U}(\theta)\Psi(r). \quad (6)$$

Let us see the transformed Schrödinger Equation under complex rotation,

$$H(r)\Psi(r) = E\Psi(r) \quad (7)$$

$$H(re^{i\theta})\Psi(re^{i\theta}) = E\Psi(re^{i\theta}) \quad (8)$$

$$\begin{aligned} H(re^{i\theta})\hat{U}(\theta)\Psi(r) &= E\hat{U}(\theta)\Psi(r) \\ \hat{U}^{-1}(\theta)H(re^{i\theta})\hat{U}(\theta)\Psi(r) &= E\hat{U}^{-1}(\theta)\hat{U}(\theta)\Psi(r) \\ \hat{U}^{-1}(\theta)H(re^{i\theta})\hat{U}(\theta)\Psi(r) &= E\Psi(r) \end{aligned} \quad (9)$$

By comparing Eq. (7) and (9)

$$\begin{aligned} H(r) &= \hat{U}^{-1}(\theta)H(re^{i\theta})\hat{U}(\theta) \quad (\text{or}) \\ \hat{U}(\theta)H(r)\hat{U}^{-1}(\theta) &= H(re^{i\theta}) = H_\theta(r) \end{aligned} \quad (10)$$

Under this transformation, the energy eigen value remains unchanged

$$H_\theta(r)\Psi_\theta(r) = E\Psi_\theta(r). \quad (11)$$

Then the asymptotic resonance wave function is transformed as

$\Psi_\theta(r) \xrightarrow[r \rightarrow \infty]{} \exp\{-(k_R \sin \theta - k_I \cos \theta)r\} \exp\{(k_R \cos \theta + k_I \sin \theta)r\}$ and oscillating with amplitude $\exp\{-(k_R \sin \theta - k_I \cos \theta)r\}$. From the above equation,

if $\tan \theta > \frac{k_I}{k_R}$, the resonance wave functions becomes

convergent at the asymptotic region.

By introducing r' as $r' = re^{i\theta}$

$$r = r'e^{-i\theta} \quad (12)$$

Eq. (11) is written as

$$H(r')\Psi(r') = E\Psi(r'). \quad (13)$$

The transformed Gaussian basis function is

$$\Psi_\theta(r) = \sum_j c_j(\theta) \exp\{-(r/b_j)^2\} \quad (\text{or})$$

$$\Psi(r') = \sum_j c_j(\theta) \exp\{-(r'/b_j e^{i\theta})^2\}$$

By using the above wave function, Eq. (13) becomes

$$H(r)\sum_j c_j(\theta) \exp\{-(r/b_j e^{i\theta})^2\} = E\sum_j c_j(\theta) \exp\{-(r/b_j e^{i\theta})^2\}$$

We have to solve the Schrödinger equation which is the same as bound state system except the range parameter b_j becomes $b_j e^{i\theta}$.

5. Numerical Calculation for Alpha-Deuteron Cluster

In our calculated energy eigen value data, we have found that the difference between resonance states and continuum states increases with increasing θ . In CRM, the continuum states vary with the 2θ dependence. Studies of resonances are indispensable for understanding the unique properties of drip-line nuclei. We have performed the α +d two-body calculation for ${}^6\text{Li}$. The positions of bound state and resonance states in the complex energy plane remains almost unchanged with the variation of rotation angle 2θ . Pauli operator is applied to push out the forbidden states between α and d clusters. The energy eigen values of ${}^6\text{Li}$ (α +d) system are shown in Table (1).

The ground state and excited states of ${}^6\text{Li}$ have been calculated as bound state and resonance states of the α -d system. All our calculated results are in good agreement with the experimental values except for the excited 2^+ resonance state of ${}^6\text{Li}$, which lies about 0.735 MeV above the experimental one (2.836 \pm 0.022 MeV). Since there are two 2^+ resonance states with different isospin ($I=0$ and $I=1$). Our interaction is independent of isospin and it is not suitable to treat isospin dependent resonance states. Moreover, These α -d interactions reproduce reasonably well the low-lying states and low-energy scattering phase shifts of the α -d systems. The ${}^6\text{Li}$ (1^+) excited state lies above the (3^+) and (2^+) excited states of ${}^6\text{Li}$. Thus calculated result of ${}^6\text{Li}$ (1^+) excited

state is not comparable with the experimental data for level width.

Table 1. The Energy Eigenvalues of ${}^6\text{Li}(\alpha+d)$ System

States	Energy level, E (MeV)		Level width, Γ (MeV)	
	Our results	Exp: results [9]	Our results	Exp: results [9]
${}^6\text{Li}$ (g.s)	-1.470	-1.474	0	stable
${}^6\text{Li}$ (3^+)	0.703	0.712 ± 0.002	0.024	0.024 ± 0.002
${}^6\text{Li}$ (2^+)	3.571	2.836 ± 0.022	1.506	1.300 ± 0.100
${}^6\text{Li}$ (1^+)	4.266	4.176 ± 0.050	3.792	1.500 ± 0.200

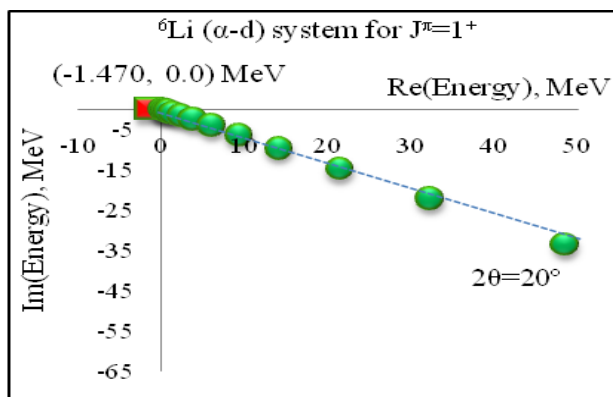


Figure 1. Energy Eigenvalue for ${}^6\text{Li}(1^+)$ State with $\theta=10^\circ$ in the Complex Plane

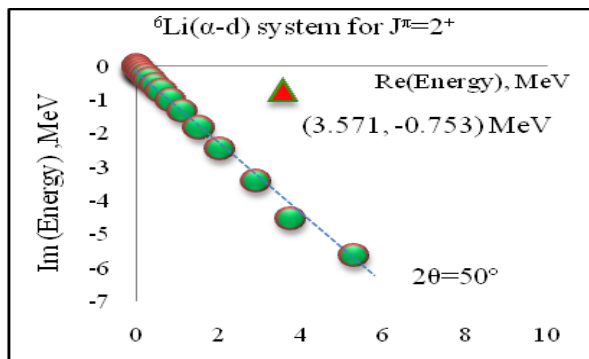


Figure 2. Energy Eigenvalue for ${}^6\text{Li}(2^+)$ with 25° in the Complex Plane

6. Pauli Suppression Effect in Three-Body System

Since alpha is a composite particle of four nucleons, Pauli exclusion effect must be included between alpha and deuteron in our formalism. The Pauli principle

characterizes the relative state between clusters in the overlapping region of them. The Pauli effect is represented by non-local potential $V_{Paul}(\vec{r}, \vec{r}')$ as

$$V_{Paul}(\vec{r}, \vec{r}') = \lim_{\lambda \rightarrow \infty} \lambda \sum_f |\phi_f(\vec{r}_{ad})\rangle \langle \phi_f(\vec{r}'_{ad})|$$

where $\phi_f(\vec{r})$ is a forbidden state.

The forbidden states are 0s and 0p between alpha and deuteron particles in ${}^7\text{Li}$.

Harmonic oscillator wave functions for 0s and 0p states are described as follows:

$$\phi_{0s}(\vec{r}) = 2\sqrt{\pi} \left(\frac{a}{2\pi}\right)^{3/4} e^{-(1/4)a\vec{r}^2} Y_{00}(\hat{r})$$

$$\phi_{0s}(\vec{R}) = 2\sqrt{\pi} \left(\frac{a}{2\pi}\right)^{3/4} e^{-a\vec{R}^2} Y_{00}(\hat{R})$$

$$\phi_{0p}(\vec{r}) = 2\sqrt{\frac{\pi}{3}} \left(\frac{a}{2\pi}\right)^{3/4} \sqrt{a} r e^{-(1/4)a\vec{r}^2} Y_{1m}(\hat{r})$$

$$\phi_{0p}(\vec{R}) = 4\sqrt{\frac{\pi}{3}} \left(\frac{2a}{\pi}\right)^{3/4} \sqrt{a} R e^{-a\vec{R}^2} Y_{1m}(\hat{R})$$

where harmonic-oscillator strength is taken to be $a=0.6947 \text{ fm}^{-2}$ for alpha. By using the channel coordinates, the matrix element of V_{Paul} can be expressed as follow:

$$\langle \Psi | V_{Paul}^{0s} | \Psi \rangle = \lim_{\lambda \rightarrow \infty} \lambda 4\pi \left(\frac{a}{2\pi}\right)^{3/2} \left(\frac{\pi}{C}\right)^{3/2} 4\pi \sum_{\ell} (2\ell+1) \int_0^{\infty} i^{\ell} r^2 e^{-Ar^2} j_{\ell}(-iDr^2) dr \quad (14)$$

$$\langle \Psi | V_{Paul}^{0p} | \Psi \rangle = \lim_{\lambda \rightarrow \infty} \lambda \frac{4\pi}{3} \left(\frac{a}{2\pi}\right)^{3/2} a \left(\frac{\pi}{C}\right)^{3/2} 4\pi \sum_{\ell} (2\ell+1) \int_0^{\infty} i^{\ell} r^4 e^{-Ar^2} j_{\ell}(-iDr^2) dr \quad (15)$$

In the Eq.(14) and (15) constants A, C and D are related to the Gaussian-basis parameters of the wave function and range parameters of the potentials. In our calculations, the strength λ is taken to be 10^8 MeV , which is large enough to push up the unphysical forbidden states in the very high energy region while keeping the physical states unchanged.

6.1 Three-Body Schrödinger Equation

The Schrödinger equation becomes

$$\left[-\frac{\hbar^2}{2\mu_c} \vec{\nabla}_{\vec{r}}^2 - \frac{\hbar^2}{2M_c} \vec{\nabla}_{\vec{R}}^2 + \left\{ V_{d\Lambda}(r_1) + V_{\alpha\Lambda}(r_2) + V_{ad}(r_3) \right\} + V_{Paul}(r_{ad}) + V_{Coul}(r_{ad}) \right] \Psi(\vec{r}, \vec{R}) = E \Psi(\vec{r}, \vec{R}) \quad (16)$$

where c is the channel, c=1, 2 and 3 which are described in Fig.(3). The relative distance vector between m_2 and m_3 is denoted by \vec{r}_1 and \vec{R}_1 is the radius vector distance between m_1 and the center of mass of m_2 and m_3 .

The total wave function of the system has

$$\Psi(\vec{r}, \vec{R}) = \sum_{c=1}^3 \sum_{ij} A_{ij}^c r_c^\ell e^{-\left(\frac{\vec{r}_c}{b_i}\right)^2} R_c^L e^{-\left(\frac{\vec{R}_c}{B_j}\right)^2} Y_{lm}(\hat{\vec{r}}) Y_{LM}(\hat{\vec{R}})$$

(17)

where b_i 's, B_j 's are range parameters and are taken as geometrical progression,

$$b_{i+1} = \left(\frac{b_N}{b_1}\right)^{1/(N-1)} b_i.$$

The geometrical progression for b_i 's are found to be useful optimizing with a small number of free parameters, N is the number of expansion coefficients and A_{ij}^c 's are expansion coefficients.

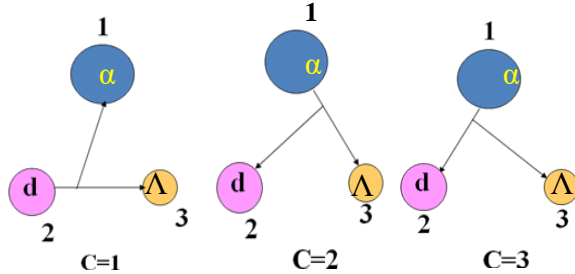


Figure. 3 Three Rearrangement Channels of the α -d- Λ System and their Jacobian Coordinate

7. Results and Discussion

7.1 Lambda Binding Energy of ${}^7\text{Li}$

We have carried out the three-body calculation to study the structure of $\alpha+d+\Lambda$ system in the coordinate space. In our calculations we have used the coupled-rearrangement channel Gaussian basis method [10]. We have calculated the binding energy of $\alpha+d+\Lambda$ three-body system by using Furutani α -d potential as well as Nishioka potential and MSA and Kurihara potentials for α - Λ interaction. We have constructed d- Λ potential phenomenologically which gives the Λ -binding energy of ${}^3\text{H}$. For ground state spin parity of ${}^7\text{Li}$, $J^\pi = 1/2^+$, we have considered the total orbital angular momentum, $\vec{L}_{\text{total}} = \vec{\ell} + \vec{\lambda} = 0$ which is obtained with $\ell = \lambda = 0, 1, 2, \dots$. We have taken into account in our calculation only $\ell = \lambda = 0$ and higher orbital angular momentum states are omitted since their contributions are very small to be negligible.

Since Pauli forbidden states between alpha and deuteron are 0s and 0p [11], we have taken into account Pauli suppression and Coulomb effect between alpha and deuteron in ${}^7\text{Li}$ ($\alpha+d+\Lambda$) system. The Λ -binding energies of ${}^7\text{Li}$ which is obtained by using the above mentioned potentials are shown in Table (2). It is found that Λ -binding energy of ${}^7\text{Li}$ with MSA is in better agreement with the experimental value than that with Kurihara potential. It is due to neglecting many-body

correlations between Λ and α particle in Kurihara potential. It is found that our calculated lambda binding energies are in fair agreement with the experimental value 5.58 ± 0.03 MeV [12]. These values are obtained by choosing the input parameters $N_1 = N_2 = N_3 = 12$ and range parameters $b_1 = 0.1$ fm and $\beta = 1.996$. It is found that the total wave function of the three-body system is sensitive to the values of the above mentioned parameters.

Table 2. Calculated Total Binding Energies and Lambda Binding Energies for ${}^7\text{Li}$ System in MeV with d- Λ Phenomenological Potential.

Λ - α interaction	α -d potential			
	Furutani potential		Nishioka potential	
	B.E	B_Λ	B.E	B_Λ
MSA	7.31	5.83	7.05	5.57
Kurihara	7.30	5.82	7.13	5.65
$B_\Lambda^{\text{exp.}} ({}^7\text{Li}) = 5.58 \pm 0.03 \text{ MeV}$ [12]				

7.2 Structural Change of the Core Nucleus

The possibility that a nuclear core shrinks when a Λ particle is added was pointed out by using the $\alpha+d+\Lambda$ cluster model for light p-shell Λ -hypernuclei. In order to see such a shrinkage effect in our analysis, we have investigated change of the relative α -d density distribution $\rho(r_{\alpha-d})$ in ${}^6\text{Li}$ and ${}^7\text{Li}$.

We have studied the relative motion between the alpha and deuteron in our three-body hypernuclear system. The relative α -d density distribution is obtained by integrating out the total wave function with \vec{R}_3 and angular parts of \vec{r}_3 i.e. \hat{r}_3 . The relative density distribution is defined as

$$\rho(r_3) = \int |\psi_{\alpha-d-\Lambda}|^2 d\vec{R}_3 d\hat{r}_3 / 4\pi \\ = (\pi/A)^{3/2} \exp\left\{-\left(a - c^2/4A\right)r_3^2\right\}$$

where constants a, c and A are related to the Gaussian-basis parameters of the wave function. It demonstrates the strong shrinkage of the $\alpha+d$ in ${}^7\text{Li}$ from that in ${}^6\text{Li}$. The obtained density distribution of the relative motion between α and d particles is displayed in Fig. (3). It can be seen that the maximum peak is found at $\alpha+d$ distance $r_{\alpha-d} = 3.2$ fm and $r_{\alpha-d} = 1.9$ fm for ${}^6\text{Li}$ and ${}^7\text{Li}$ respectively. In ${}^6\text{Li}$, the bound state solution of the $\alpha+d$ system has one node, lacking of the 0s type solution. It indicates that the relative wave function is orthogonal to the 0s forbidden state.

We also calculated the r.m.s distance between alpha and deuteron in three-body calculation. It is defined as

$$\tilde{r}_{\alpha d} = \left[4\pi \int r_3^2 \rho(r_3) r_3^2 dr_3 \right]^{1/2}$$

$$\tilde{r}_{\alpha d} = \left[\frac{3\pi^3 A}{2(aA - c^2/4)^{5/2}} \right]^{1/2}.$$

Our calculated r.m.s distance of $\alpha+d$ in ${}_{\Lambda}^7Li$ is found to be 3.44 fm which is significantly smaller than that of $\alpha+d$ in 6Li which is 4.1 fm. We can see clearly that the ground state of $\alpha+d$ core nucleus is changed due to the participation of Λ particle. One of the reasons why this drastic shrinkage happens is that the Λ particle is out of the antisymmetrization and can stay deeply inside the core nucleus to gain deeper binding energy.

This shrinkage effect is seen in the large change of the expectation value of the relative kinetic energy, $\langle T_{\alpha d} \rangle$, and that of the potential energy, $\langle V_{\alpha d} \rangle$, in the $\alpha+d$ subsystem. When the α and d clusters approach to each other, the increase of $\langle T_{\alpha d} \rangle$ overcomes the gain of the $\langle V_{\alpha d} \rangle$, and the sum $\langle T_{\alpha d} + V_{\alpha d} \rangle$ increases appreciably. In spite of this energy loss in the $\alpha+d$ core system, the core shrinkage is realized by the stronger energy gain of the $\Lambda-\alpha$ and $\Lambda-d$ parts.

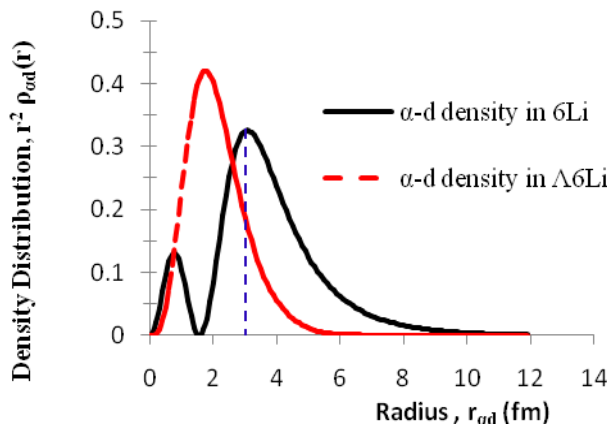


Figure. 3 The Density Distribution of Relative Motion between α -d

Table 3. Calculated r.m.s Distances of Core Nucleus, Expectation Value of Kinetic Energy and Potential Energy between α -d in 6Li and ${}_{\Lambda}^7Li$.

System	$\tilde{r}_{\alpha d}$	$\langle T_{\alpha d} \rangle$	$\langle V_{\alpha d} \rangle$	$\langle T_{\alpha d} + V_{\alpha d} \rangle$
6Li	4.11	11.59	-13.06	-1.47
${}_{\Lambda}^7Li$	3.44	15.59	-16.70	-1.11

8. Conclusion

In this paper, one Λ particle is added to 6Li nucleus with weakly-bound state, a resultant hypernucleus ${}_{\Lambda}^7Li$ becomes more stable. It is due to the glue-like role of an attracted Λ particle. Moreover structural change of the $\alpha+d$ nuclear core by the participation of the Λ particle is seen in ${}_{\Lambda}^7Li$ hypernucleus, which is about 16% shrinkage of the r.m.s distance $\tilde{r}_{\alpha d}$ in ${}_{\Lambda}^7Li$ compared to that $\tilde{r}_{\alpha d}$ in 6Li . Thus we conclude that glue like role of the Λ -particle is important to study the Λ -Hypernucleus.

9. Acknowledgement

Authors would like to thank Prof. Y. Akaishi, RIKEN Nishina Center, Wako in Japan for his fruitful discussions on this research work.

10. References

- [1] Bohr A., “On the Quantization of Angular Momenta in Heavy Nuclei”, Phys. Rev. 81 (1951) 134.
- [2] Furutani H. et al., “Study of non-alpha nuclei based on the viewpoint of cluster correlation”, Prog. Theor. Phys. Suppl. 68 (1980) 193.
- [3] Nishioka, H. S. Saito and M. Yasuno, “Ab initio calculations of amplitude and phase functions for extended x-ray absorption fine structure spectroscopy”, Prog. Theor. Phys. 62 (1979) 424.
- [4] Akaishi Y., K.S. Myint and S. Shinmura, “Central Repulsion of $\Lambda-\alpha$ Interaction with Hard-Core $\Lambda-N$ Potential”, Eur. Phys.J. A 16 (2003) 21.
- [5] Nagels M., T.A. Rijken, J.J. de Swart, “Baryon-baryon scattering in a one-boson-exchange-potential”, Phys. Rev. D 15 (1977) 2547.
- [6] Kurihara Y. et al., “Central Repulsion of $\Lambda-\alpha$ Interaction with Hard-Core $\Lambda-N$ Potential”, Prog. Theor. Phys. Vol. 71 (1984) 561.
- [7] Bertini R. et al., “Hypernuclei with sigma particles”, Phys. Lett. B 83 (1979) 306.
- [8] Gyarmati B. and A.T. Kruppa, “Complex scaling in the description of nuclear resonances”, Phys. Rev. C34 (1985) 1.

- [9] Tilley D.R. et al., “Energy Levels of Light Nuclei”, Nucl. Phys. A745 (2004) 155.
- [10]Kamimura M., “Nonadiabatic coupled-rearrangement-channel approach to muonic molecules”, Phys. Rev. A 38 (1987) 622.
- [11] Kukulin V.I., et al., “Detailed study of the cluster structure of light nuclei in a three-body model (IV). Large space calculation for $A = 6$ nuclei with realistic nuclear forces”, Nucl. Phys. A 586 (1995) 151.
- [12] Bertini R. et al., “A full set of nuclear shell orbitals for the Λ particle observed in $\Lambda^{32}\text{S}$ and $\Lambda^{40}\text{Ca}$ ”, Phys. Lett. B 83 (1979) 306.

Detection of a Single- Λ Hypernucleus by K^- Meson Interaction with Nuclear Emulsion

Htaik Nandar Kyaw¹, Thida Wint²

Lecturer¹, Associate Professor²

Department of Physics^{1,2}

Defence Services Academy¹, Mandalay University of Distance Education²

kyawhtaiknandar@gmail.com¹, thidarwint@gmail.com²

Abstract

In this research, a single- Λ hypernucleus event which is detected in overall scanning of KEK-PS E373 Hybrid-Emulsion Experiment is analyzed by using kinematical analysis. The event is observed by the incident K^- meson interaction with emulsion nucleus. Firstly, all possible decay modes of analyzed single- Λ hypernucleus are chosen and their Q -values are calculated. Moreover, the momentum and kinetic energy of all emitted charged particle decay products are calculated by Range-Energy relation calculation package. Finally, the possible masses of single- Λ hypernucleus are calculated by mass-energy relation. According to our analysis, a single- Λ hypernucleus is identified as either ${}^5_A He$ or ${}^6_A He$.

Keywords- single- Λ hypernucleus, nuclear emulsion, overall scanning, range-energy relation, mass-energy relation

1. Introduction

Hypernuclei are nuclei which consist of nucleons and one or more hyperons. Hyperons are unstable strange particles with a mean lifetime of the order of 10^{-10} s. In the family of hyperons, Λ is the lightest particle and it can stay in contact with nucleons inside nuclei and form hypernuclei. A hypernucleus which is made up of nucleons and one Λ hyperon is called a single- Λ hypernucleus. If a nucleus composed of protons, neutrons and two Λ hyperons, it is said to be a double- Λ hypernucleus. If two single- Λ hypernuclei are produced simultaneously it is called a twin- Λ hypernucleus. The abundant source of hypernuclei is nuclear emulsion. It is a type of three dimensional detector of photographic plate which is used to record the true rectified range of charged particles. A hypernucleus can be seen as a track in nuclear emulsion.

Theoretical purpose of hypernuclear physics is to complete the knowledge of baryon-baryon interactions in a unified way. To do so, it is essential to understand the $N-N$, $\Lambda-N$, $\Lambda-\Lambda$ and $\Xi-N$ interactions which can be extracted from ordinary nuclei, single- Λ hypernuclei, double- Λ hypernuclei and twin- Λ hypernuclei. Moreover, experimental motivation of hypernuclei is to draw the three dimensional nuclear chart with one axis

being strangeness. Observation of hypernuclei in nuclear emulsion will give significant contribution to strangeness -1 and -2 sectors of nuclear chart. To fulfil both theoretical and experimental purposes, the most important things are to observe more and more hypernuclei events and to identify the observed events kinematically. Therefore, hypernuclei searching experiments KEK-PS E176 and E373 are carried out at Japanese High Energy Accelerator Research Organization using hybrid-emulsion method [1]. In this paper, a single- Λ hypernucleus of KEK-PS E373 experiment which is observed in overall scanning of nuclear emulsion is analyzed using kinematical analysis and detailed analyses are presented.

2. Analysis of a Single- Λ Hypernucleus Event

In this section, a single- Λ hypernucleus event which is observed in KEK-PS E373 experiment is analyzed kinematically. The event is observed in overall scanning of E373 experiment. In E373 experiments, semi-automatic scanning is firstly used to search hypernuclei events. In order to observe more hypernuclei events, E373 experiment had developed a new scanning method called "overall scanning" to speed up the detection of hypernuclei events in emulsion rapidly. In overall scanning method, a computer controlled microscope scans the entire volume of emulsion plates exhaustively.

2.1. Description of Analyzed Event

The photograph and schematic diagram of analyzed single- Λ hypernucleus event are presented in figure 1 and 2. The event is observed by the incident K^- meson interaction with emulsion nucleus at point A and emulsion star including hypernucleus track #1 is emitted. At point B, a hypernucleus track #1 decays into three charged particle tracks #2, #3 and #4. According to the ionization measurement [2], the charged particle track #4 is identified as π^- meson. Moreover, the kinetic energy of track #4 is calculated by using $13805.5 \mu\text{m}$ ranges in nuclear emulsion and the calculated kinetic energy of track #4 is 27.312 MeV . This result is consistent with the kinetic energy of π^- particles which were observed in other hypernuclear events [3].

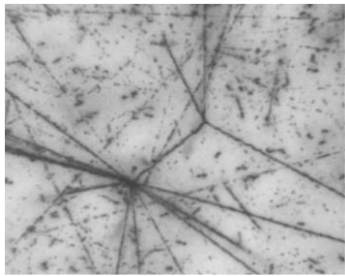


Figure 1. Photograph of Analyzed Event

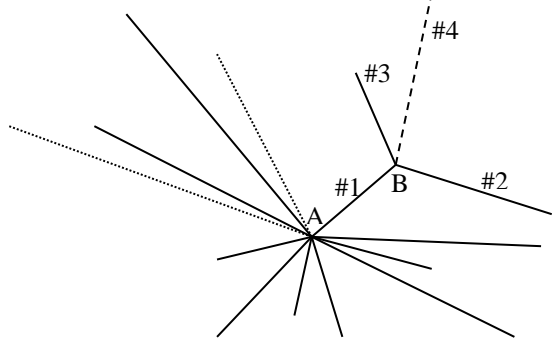


Figure 2. Schematic Diagram of Analyzed Event

The measured ranges and position angles of emitted charged particle tracks are presented in table 1.

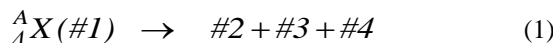
Table 1. Measured Ranges and Position Angles of Track #1, #2, #3 and #4

Point	Track	R (μm)	θ (degree)	ϕ (degree)
A	#1	16.4 ± 0.8	74.6 ± 0.1	109.5 ± 0.2
B	#2	27.2 ± 0.9	156.2 ± 0.5	143.0 ± 1.0
	#3	16.3 ± 0.2	138.5 ± 0.2	322.1 ± 0.3
	#4	13805.5 ± 2.9	147.6 ± 0.1	232.2 ± 0.1

The charged particles tracks #2, #3 and #4 lie in the same plane that is three tracks are coplanar. So, it is assumed that, there is no neutron emission at vertex point B and possible decay modes which consist of only charged particle tracks are considered.

2.2. Possible Decay Modes at Point B

At point B, a single- Λ hypernucleus track #1 decays into three charged particles track #2, #3 and #4 such as



The ionization measurement and range-energy relation determined the charged particle track #4 as a π^- . Due to coplanarity of three tracks, neutron emission doesn't need to consider in this decay and the following (17) possible decay modes are obtained.

Table 2. Possible Decay Modes at Point B

No.	Decay Modes
1	${}^3_AH \rightarrow {}^2_1H + {}^1_1H + \pi^-$
2	${}^3_AH \rightarrow {}^1_1H + {}^2_1H + \pi^-$
3	${}^4_AH \rightarrow {}^3_1H + {}^1_1H + \pi^-$
4	${}^4_AH \rightarrow {}^2_1H + {}^2_1H + \pi^-$
5	${}^4_AH \rightarrow {}^1_1H + {}^3_1H + \pi^-$
6	${}^4_AHe \rightarrow {}^3_2He + {}^1_1H + \pi^-$
7	${}^4_AHe \rightarrow {}^1_1H + {}^3_2He + \pi^-$
8	${}^5_AHe \rightarrow {}^4_2He + {}^1_1H + \pi^-$
9	${}^5_AHe \rightarrow {}^1_1H + {}^4_2He + \pi^-$
10	${}^5_AHe \rightarrow {}^3_2He + {}^2_1H + \pi^-$
11	${}^5_AHe \rightarrow {}^2_1H + {}^3_2He + \pi^-$
12	${}^6_AHe \rightarrow {}^5_2He + {}^1_1H + \pi^-$
13	${}^6_AHe \rightarrow {}^1_1H + {}^5_2He + \pi^-$
14	${}^6_AHe \rightarrow {}^4_2He + {}^2_1H + \pi^-$
15	${}^6_AHe \rightarrow {}^2_1H + {}^4_2He + \pi^-$
16	${}^6_AHe \rightarrow {}^3_2He + {}^3_1H + \pi^-$
17	${}^6_AHe \rightarrow {}^1_1H + {}^3_2He + \pi^-$

2.3. Calculation of Q-values at Point B

In order to check the possible decay modes of table 1 are allowed or forbidden, the Q-values for all possible decay modes are calculated. Q-value is defined as the energy released or absorbed during the nuclear reaction. If the calculated Q-value is positive, it is defined as exoergic reaction and the reaction is energetically possible. So, the reaction is allowed and is taken into consideration to perform analysis.

If the calculated Q-value is negative, it is defined as endoergic reaction and the reaction does not energetically possible. So, the energy must be supplied to incident particle to complete the reaction. But the life time of Λ hypernucleus is about 10^{-10}s and the reaction or decay of hypernucleus should be energetically possible in nuclear emulsion.

For the hypernuclear decay processes at point B, the Q-value becomes

$$Q(\text{MeV}) = [M(\#1) - \{M(\#2) + M(\#3) + M(\#4)\}]c^2 \quad (2)$$

In equation 2, the masses of hypernucleus track #1 and that of charged particles track #2, #3 and #4 are expressed in MeV/c^2 unit. According to our calculation, the

calculated Q-values are all positive and those decay modes are energetically possible. Therefore, (17) possible decay modes of table 1 are taken into considerations to perform our analysis. Our results will be summarized in table 3.

2.4. Calculation of Total Kinetic Energy (E_{total}) of Charged Particles at Point B

In nuclear emulsion, event identification of hypernuclei is based on the conservation laws of energy and momentum, and the mass of hypernuclei are calculated from the energies of their decay daughters. Since the kinetic energy of a charged particle is obtained by measuring its range. So, the range-energy relation is quite important for emulsion analysis. In the present research, kinetic energies of charged particles tracks #2, #3 and #4 in nuclear emulsion are calculated by Range-Energy Relation Calculation Package which is supported by spokesperson of KEK-PS E373 experiment [4]. This package is written by Visual Fortran program Code and is also based on the traditionally used range-energy formula in nuclear emulsion [5] such as

$$R = R_I + R_2 = \frac{R_s / F}{Z^2(M_p M_{\text{mass}})} + \frac{M}{R_{\text{ext}}} \quad (3)$$

where, $R_I = \frac{R_s / F}{Z^2(M_p M_{\text{mass}})}$ is the measured range. In

this equation, $\frac{R_s}{F}$ is range straggling of proton,

$$F = \frac{RR \times D - 1}{RR \times D_0 - 1} + \frac{RR(D_0 - D)}{RR \cdot D_0 - 1} \cdot \frac{R_s}{R_w} \quad \text{is range of a proton}$$

at velocity β , RR is ratio of the volume increment in cubic centimeters to the weight increment in grams, D is emulsion density, D_0 is density of standard emulsion, R_s is proton range in standard emulsion and R_w is proton range

in water. In the second term, $R_2 = \frac{M}{R_{\text{ext}}}$ is the range of correction of track ends.

Here, $R_{\text{ext}} = M_z^{2/3} C_z$ is the range of electrons captured by the positive charged ions, C_z is a unique function of β/z , independent of the species of the incident particle and β is the velocity of the incident particle relative to the velocity of light. The sum of kinetic energies of three charged particles for each decay mode is called total kinetic energy and we calculated this energy in this section. If neutral particles are emitted, E_{total} should be less than Q-value because neutral particles cannot be seen or measured in nuclear emulsion. If charged particles are emitted, E_{total} should be equal to Q-values. According to our calculation, the selected seventeen possible decay modes have total kinetic energy comparable to Q-values. Our calculated total kinetic energies are compared with Q-values and the results are summarized in table 3.

The calculated total kinetic energy and calculated Q-values are comparable but ${}^5He \rightarrow {}^4He + {}^1H + \pi^-$ and ${}^6He \rightarrow {}^1H + {}^5He + \pi^-$ decay modes have most probable results.

2.5. Calculation of Mass of Hypernucleus Track #1 at Point B

In the previous sections, the possible decay modes of single- Λ hypernucleus at point B are chosen, the Q-values of all possible decay modes are calculated and the total visible energy released for all possible decay modes are also calculated. In this section, the possible masses of single- Λ hypernucleus track #1 are calculated by extracting the kinetic energy of charged particle decay products at point B. At point B, a single- Λ hypernucleus decays mesonically into three charged particles. The possible masses of single- Λ hypernucleus can be calculated by using the formula,

$$\sum_{i=1}^n M_i c^2 = \left[\sum_{i=1}^n (T_i + M_i) \right] \quad (4)$$

In the equation 4, M is the mass of single- Λ hypernucleus, T_i is the kinetic energy and M_i is the rest mass energy of i^{th} decay product. The calculated masses of a single- Λ hypernucleus for all possible decay modes at point B are presented in table 3. According to our calculation, the calculated results for all possible decay modes are within the acceptable range compare with the known mass of hypernuclei and the species of hypernucleus track #1 cannot identify using only mass data.

3. Results and Discussions

The calculations only total kinetic energy (or) only possible masses cannot be identified the species of single- Λ hypernucleus. Therefore, the calculated Q-values, total kinetic energies of charged particles, calculated masses of single- Λ hypernucleus and known masses of single- Λ hypernucleus from particle data group for each decay mode are compared in table 3 to get the more precise results.

According to table 3, it is found that the calculated Q-values are very consistent with total kinetic energy in ${}^5He \rightarrow {}^4He + {}^1H + \pi^-$ and ${}^6He \rightarrow {}^1H + {}^5He + \pi^-$ decay modes. The Q-value for ${}^5He \rightarrow {}^4He + {}^1H + \pi^-$ is 34.661 ± 0.053 MeV and that of total kinetic energy is 34.315 ± 0.205 MeV. For ${}^6He \rightarrow {}^1H + {}^5He + \pi^-$ decay mode, the calculated Q-value is 33.601 ± 0.071 MeV and that of total kinetic energy is 33.196 ± 0.107 MeV. If there is neutron emission, the total kinetic energy should be less than Q-value. If there is only charged particle emission, the visible energy released should be equal to Q-value by mass energy conservation law.

Table 3. Comparison of Calculated Results at Point B for all Possible Decay Modes

Possible Decay Modes	Q (MeV)	E _{total} (MeV)	Mass (MeV/c ²)	Known Mass of PDG (MeV/c ²)
$^3_A H \rightarrow ^2_I H + ^1_I H + \pi^-$	37.651 ± 0.070	30.337 ± 0.063	2983.815 ± 0.100	2991.127 ± 0.071
$^3_A H \rightarrow ^1_I H + ^2_I H + \pi^-$	37.651 ± 0.070	30.199 ± 0.055	2983.815 ± 0.100	2991.127 ± 0.071
$^4_A H \rightarrow ^3_I H + ^1_I H + \pi^-$	35.741 ± 0.063	30.597 ± 0.071	3917.388 ± 0.068	3922.532 ± 0.064
$^4_A H \rightarrow ^2_I H + ^2_I H + \pi^-$	31.708 ± 0.063	30.602 ± 0.222	3921.426 ± 0.068	3922.532 ± 0.064
$^4_A H \rightarrow ^1_I H + ^3_I H + \pi^-$	35.741 ± 0.063	30.357 ± 0.068	3917.388 ± 0.068	3922.532 ± 0.064
$^4_A He \rightarrow ^3_I He + ^1_I H + \pi^-$	35.391 ± 0.057	33.794 ± 0.182	3920.045 ± 0.061	3921.642 ± 0.058
$^4_A He \rightarrow ^1_I H + ^3_2 He + \pi^-$	35.391 ± 0.057	32.642 ± 0.096	3920.045 ± 0.061	3921.642 ± 0.058
$^5_A He \rightarrow ^4_2 He + ^1_I H + \pi^-$	34.661 ± 0.053	34.315 ± 0.205	4839.571 ± 0.056	4839.917 ± 0.054
$^5_A He \rightarrow ^1_I H + ^4_2 He + \pi^-$	34.661 ± 0.053	32.958 ± 0.102	4839.571 ± 0.056	4839.917 ± 0.054
$^5_A He \rightarrow ^3_I He + ^2_I H + \pi^-$	16.318 ± 0.053	34.057 ± 0.186	4857.656 ± 0.056	4839.917 ± 0.054
$^5_A He \rightarrow ^2_I H + ^3_2 He + \pi^-$	16.318 ± 0.053	33.045 ± 0.110	4857.656 ± 0.056	4839.917 ± 0.054
$^6_A He \rightarrow ^5_I He + ^1_I H + \pi^-$	33.601 ± 0.071	34.737 ± 0.223	5780.464 ± 0.132	5779.328 ± 0.122
$^6_A He \rightarrow ^1_I H + ^5_2 He + \pi^-$	33.601 ± 0.071	33.196 ± 0.107	5780.464 ± 0.132	5779.328 ± 0.122
$^6_A He \rightarrow ^2_I H + ^5_I He + \pi^-$	36.724 ± 0.121	34.578 ± 0.209	5777.182 ± 0.132	5779.328 ± 0.122
$^6_A He \rightarrow ^1_I H + ^5_2 He + \pi^-$	36.724 ± 0.121	33.361 ± 0.116	5777.182 ± 0.132	5779.328 ± 0.122
$^6_A He \rightarrow ^3_I He + ^3_I H + \pi^-$	22.414 ± 0.121	34.215 ± 0.188	5791.129 ± 0.132	5779.328 ± 0.122
$^6_A He \rightarrow ^3_I H + ^2_2 He + \pi^-$	22.414 ± 0.121	33.303 ± 0.122	5791.129 ± 0.132	5779.328 ± 0.122

So, $^5_A He \rightarrow ^4_2 He + ^1_I H + \pi^-$ and

$^6_A He \rightarrow ^1_I H + ^5_2 He + \pi^-$ decay modes have no neutron emission and only charged particle decay products are observed at point B. Their Q-values and visible energy released are very consistent. Moreover, the calculated mass of $^5_A He$ hypernucleus is 4839.571 ± 0.056 MeV/c² for $^5_A He \rightarrow ^4_2 He + ^1_I H + \pi^-$ decay mode. The known mass of $^5_A He$ from particle data group is 4839.917 ± 0.054 MeV/c². Furthermore, the calculated mass of $^6_A He$ hypernucleus is 5780.464 ± 0.132 MeV/c² for $^6_A He \rightarrow ^1_I H + ^5_2 He + \pi^-$ decay mode and that of particle data group is 5779.328 ± 0.122 MeV/c². So the calculated masses values are also consistent with known masses of particle data group.

Due to the above physical processes, a single- Λ hypernucleus event is successfully identified as $^5_A He$ (or) $^6_A He$ using its decay point and the following two decay modes are chosen as the acceptable decay modes.

- (i) $^5_A He \rightarrow ^4_2 He + ^1_I H + \pi^-$
- (ii) $^6_A He \rightarrow ^1_I H + ^5_2 He + \pi^-$

4. Conclusion

The KEK-PS E373 Hybrid-Emulsion experiment has been carried out at 12 GeV Proton Synchrotron of Japanese High Energy Accelerator Research Organization (KEK). The aim of this experiment is to study strangeness hypernuclei with ten times higher statistics than previous experiment KEK-PS E176. In this experiment, seven double- Λ hypernuclei, two twin- Λ hypernuclei and 46 single- Λ hypernuclei are observed during the semi automatic scanning of Ξ^- candidate events. To observe more hypernuclei events in nuclear emulsion, a new scanning method which is called overall scanning is introduced in this experiment and several hypernuclei events with two vertex points are detected.

In this research paper, a single- Λ hypernucleus event which is observed in overall scanning of nuclear emulsion is analyzed. The event is detected by K meson interaction with nuclear emulsion and forming an emulsion star. In this research kinematical analysis is used to identify hypernucleus event. Kinematical analysis is an analysis which is performed by using physical quantities due to particles' motion such as range, velocity, momentum and kinetic energy, etc. After detecting the hypernucleus events in nuclear emulsion, we can measure the range and position angles of charged particle tracks only. Using the relativistic kinematics, kinetic energy, velocity, momentum, mass, binding energy and interaction energy can be derived. So many physical quantities will be obtained using the range data only. According to our analysis, a single- Λ hypernucleus event is successfully identified as $^5_A He$ (or) $^6_A He$ using its decay point and the two decay modes such as $^5_A He \rightarrow ^4_2 He + ^1_I H + \pi^-$ and $^6_A He \rightarrow ^1_I H + ^5_2 He + \pi^-$ are chosen as the acceptable decay modes.

Nowadays, nuclear emulsion experiments play an important role to search and analyze the hypernuclei which contain strange quark. After observing the hypernuclei events, one cannot identify the species of hypernuclei without doing analysis. This paper significantly shows the importance of kinematical analysis to identify the hypernuclei events observed in nuclear emulsion. From our analysis, we can provide some useful data to hypernuclear research groups to extend the three dimensional strangeness nuclear chart.

5. References

- [1] K. Nakazawa, “Double- Λ Hypernuclei via the Ξ^- Hyperon Capture at Rest”, *Nuclear Physics A 835*, Elsevier Print, ISSN03759474, Netherlands, 2010, Page 207-214.
- [2] M. Sweet, “*Measurement of the lifetime of Light Single hypernuclei ($A<5$) in nuclear emulsion of the E373 experiment*”, Graduate School of Engineering, Gifu University, Gifu, Japan, 2016.
- [3] H. Takahashi and K. Nakazawa, “Experimental Study of Double- Λ Hypernuclei with Nuclear Emulsion”, *Progress of Theoretical Physics Supplement 185*, Oxford University Press, 2010, Page 335-343.
- [4] K. Nakazawa, Private Communication
- [5] A. Ichikawa, “*Study of S=-2 Nuclear Systems with Hybrid Emulsion Method*”, PhD Thesis, Kyoto University Print, Kyoto, Japan, 2001.

Experimental Design of Fan-beam Gamma Computed Tomography based on Single-source and Single-detector Scanning System for Industrial Application

Saw Nyi Nyi Zaw¹, Myo Zaw Htut², Than Tun Aung³, Khaing Nyunt Myaing⁴, Kyaw Lin Oo⁵

Department of Nuclear Physics^{1, 2, 3, 4, 5}

Defence Services Academy^{1, 2, 3, 4, 5}

*sawnyinyi539@gmail.com¹, mzhtut@gmail.com², chitnyalay@gmail.com³, khaing.nm@gmail.com⁴
kyawlino53@gmail.com⁵*

Abstract

This paper focus on the new experimental design for third-generation fan-beam CT based on single-source and single-detector scanning system with data acquisition and control system for CT scan measurement, 2D image reconstruction and 3D volume visualization and structural analysis. The Lab-scaled industrial CT scanning system has been designed based on fan-beam system with control system in Nuclear Physics Laboratory, DSA. In this research work also developed the program with data acquisition system of combining with the detection control and motion control systems using Arduino microcontroller board with Adafruit motor driver and Cassy modules in MATLAB GUI. The proposed CT system can be used for improving design, investigating and optimization in many industrial applications and process controls.

Keywords- Gamma Computed Tomography, Fan beam, Arduino UNO, Control system, CASSY Modules and MATLAB GUI.

1. Introduction

Computed Tomography (CT) is a powerful tool capable of inspecting external and internal structures in many industrial applications as well as providing information with very high accuracy. For design and construction of an industrial computed tomography (ICT) system in particular application need to consider the effective cost and reliable enough for the intended purpose [1]. Design for industrial CT is different and consideration varies in portable and permanently fixed CT system. For field application industrial computed tomography system can be design by user to specific application [2]. According to the experiences of the CT application in various industrial environments the application CT design must be simplicity and accuracy for the measurement system. The control system in CT plays the main part in positional motion and detection accuracy for acquiring reconstruction data and data acquisition in tomographic system also relates high accuracy and good repeatability. In this work, some of new experimental design and the development of industrial CT system are presented.

2. Aim

The aim of this work is the design and construction of third generation fan-beam Gamma Computed Tomographic Scan (GCTS) system with single source and single detector for CT scan measurement, 2D and 3D structural analysis for industrial field applications.

3. Theory Background

3.1 Principle of Fan-Beam Gamma CT

Tomography systems based on transmissions and emissions of gamma-ray have been developed in recent years. In a gamma-ray transmission CT, the transmitted intensity, I , of a mono-energetic radiation beam traversing an object of thickness x given by the following equation:

$$I = I_0 e^{-\int \mu(x,y) dx dy} \quad (1)$$

Where, I_0 is the incident beam intensity of the radiation beam and $\mu(x, y)$ is the linear attenuation coefficient. Equation (1) can be rearranged as follows:

$$\ln \frac{I_0}{I} = \int \mu(x, y) dx dy \quad (2)$$

The method of data collection would be to rotate the radiation source around the object and sample a complete fan of projection on the detector at each position. The rays of the fan are sampled in equiangular intervals, i.e. they are measured at equidistant intervals on a circular position of detector.

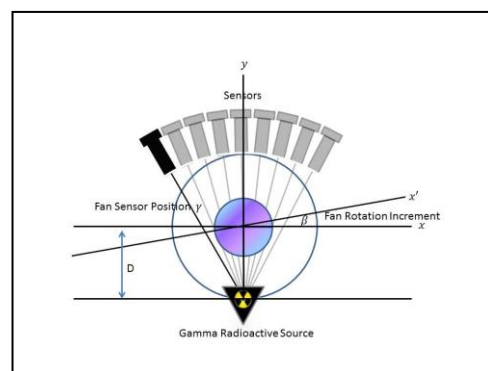


Figure 1. The Fan-Beam Geometry System

The rotation angle of the source with respect to the y-axis of the coordinate system will be denoted by β , the angle between a specific projection ray and the central ray of the fan will be denoted by γ . Figure 1 shows the acquisition parameters for the projection in the fan beam data set (β, γ) . The transformation is given by $\theta = \beta + \gamma$ and $t = D \sin \gamma$.

The line integral along the path of μ is known as the Ray-sum. In figure 1, $p(\beta, \gamma)$ is the line integral of $\mu(x, y)$ along a line inclined from the point of origin [2]. Mathematically, it is written as follows [3]:

$$p(\beta, \gamma) = \int \mu(x, y) dx dy \quad (3)$$

3.2 Image Reconstruction and Visualization for Fan-Beam Gamma CT

The reconstruction algorithms using in Industrial Computed Tomography (ICT) are derived from the base of Medical Imaging Technique (MIT). In other words, ICT and MIT are different in scanning objects and purposes, but they almost used the same algorithms to reconstruct. The image reconstruction in CT measurement currently used the analytical algorithms: simple Back Projection (BP) and Filter Back Projection (FBP) methods [4]. The reconstructed images by different projection in BP and FBP methods with different filters and interpolations. From the transmitted measured data, tomographic images were reconstructed by GCTS image reconstruction program in MATLAB [5]. The advanced imaging techniques such as CT produce enough data to display volumetric visualization, because CT slice has the dimensions of depth (slice thickness), the pixel is transformed into a voxel. In MATLAB can be applied codes for 3D surface visualization such as squeeze, smooth3, patch, isosurface, isocap and sub volume are used for volume visualization [6]. Moreover, 3D image visualization program was developed by creating the 3D volume data from multi-slices 2D reconstructed image data in MATLAB [6].

4. Experimental Work

4.1 Designs for Fan-Beam Gamma CT

According to the field applicability, more expensive and heavy CT system is not always impossible. From the experiences in various industrial environments, it was occurs that a system needs to be as simple as possible because of not only the cost for fabrication but also for its portability and adaptability in field applications. For these purpose we have been designed the third generation fan-beam Gamma Computed Tomographic Scan (GCTS) system with single source and single detector. And therefore Lab-scaled experimental design of GCTS system is constructed in Nuclear Physics Laboratory, Department of Nuclear Physics at D.S.A. The conceptual experimental design

for field application and Lab-scaled experimental design of GCTS system are shown in figure 2.

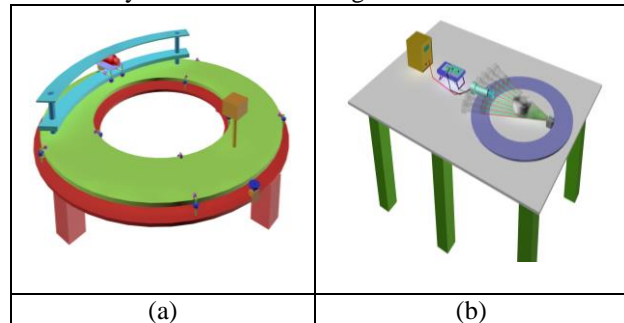


Figure 2. Fan-beam GCTS System (a) Experimental Design for Field Application and (b) Lab-scaled Experimental Design

4.2 Experimental Setup of Lab-scaled Fan-Beam Gamma CT System

Experimental design of GCTS system is the third generation of Industrial Computed Tomography system based on gamma transmission method and the fan-beam geometry with single-source and single-detector scanning system. This system was designed for fan-beam scanning system with arc geometry and experimental setup of this system is represented in figure 3.



Figure 3. Experimental Setup of Lab-scaled GCTS System

The Lab-scaled GCTS system was constructed at Defence Services Academy and also created GCTS program for this system in MATLAB GUI [7]. Lab-scaled CT system was set up to be able to move rotational motion on the scanning object material. In this CT system, radioactive sources were 2.6 MBq of Cs-137 for low and medium density object materials and 88 MBq of Co-60 for high density object materials and the detector was 1x1 inch NaI (Tl) scintillation detector, shielded by lead collimator with (8x6.8x1) cm and hole-diameter with 1 cm respectively. Radiation source and detectors were fixed in opposite alignment to measure the transmitted gamma-ray through the scanning object. In this system, the object was rotated to be scanned at different angles and the detector was also rotated at different angular positions to acquire the data for the required projections. Measurements were performed with maximum distance 70 cm and maximum beam angle 60 ° of source to detector and scanning object with 25 cm in maximum diameter.

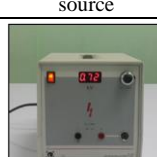
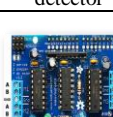
		
Sample	Cs-137 gamma source	Lead collimator
		
Scintillation detector	High voltage power supply	Sensor-CASSY with MCA box
		
Adafruit Motor Shield	Arduino UNO	Stepper Motor

Figure 4. Assemblies of Lab-scaled GCTS System

In this research work the analysis and application programs were created for gamma transmission measurement using with CASSY-modules and MATLAB GUI. The gamma-ray intensity profile with default projections has been measured by GCTS measurement program.

4.3 Control System for Fan-Beam Gamma CT

For the accurate measurement for industrial field applications we have developed prototype control system the motion of scanner with the 2 stepper motors by using Adafruit Motor Driver and Arduino Uno microcontroller board. And this control system performed the control of detection system of NaI (Tl) detector with MCA, high voltage and CASSY sensor via USB. This system is also controlled with the combination of the arrangement of samples and detector motions by MATLAB based GCTS measurement program. The scanning process is driven by 2 stepper motors (M1 and M2). The first motor M1 is used to rotate step by step the detector with arc angle 0.9° to 7.2° for maximum 64 projections. The second motor M2 is drive to rotate the object sample with angle 0.9° to 360° for maximum 400 projections. The control system motion and detection in GCTS system is represented in figure 5.

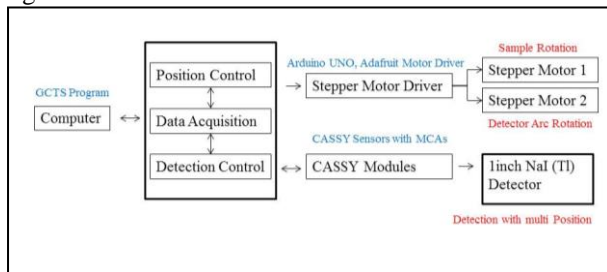


Figure 5. Control System of Lab-scaled GCTS System

4.4 Program Implementation for Lab-scaled Fan-Beam Gamma CT

In this research work Lab-scaled version of GCTS program has been created by MATLAB GUI package based on CASSY modules. GCTS program includes three main subprograms: measurement program, 2D image reconstruction program and 3D volume visualization program as following:

Measurement Program: This program operated gamma transmission measurements with control of detection system and mechanical control system. In the measurement program of gamma-ray CT system firstly load and read the digital data from MCA box with CASSY sensor of detecting assembly for current measurement with default parameters such as projection angle and step of detector position. After that the program records the count in each channel in every second for the whole measurements. After completion of measurements for the whole object, the intensity profile was saved as a ray-sum in (*.mat). The interface of measurement program represents in figure 6.

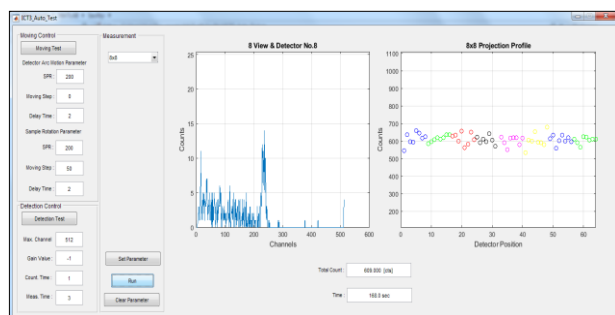


Figure 6. The Interface of GCTS Measurement Program

The measured spectrum was calibrated with energy of gamma radiation source, which was used in the measurement, and executed as the energy spectrum file. After calibration the energy spectrum file was saved in current measurement and calculated the intensity with region of interest (ROI) of photo peak in measured spectrum. Image Reconstruction Program: This program generates the intensity images, which was related to the density distribution of object based on gamma-ray attenuation. This program loads the measured intensity profile (energy spectrum file) and initializes the data and then creates intensity profile, projection data and sinogram data. In this program have been used the simple back projection (BP) and filtered back projection (FBP) based on radon and inverse radon transforms with different filters and interpolation functions for image reconstruction [5]. Moreover, in this program developed the tools for image information appearance, image zooming in and out, panning, adjustment of the window level and width, adjustment of contrast,

cropping, distance measurement, conversion of the image to a pixel matrix and color map choices. The interface for image reconstruction program is illustrated in figure 7.

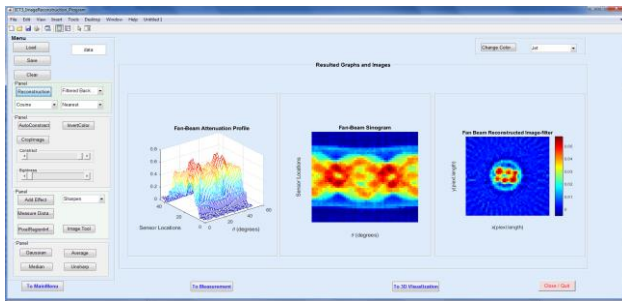


Figure 7. The Interface of GCTS Reconstruction Program

3D Volume Visualization Program: This program was developed by creating the 3D volume data from multi-slices 2D reconstructed image data of various CT scan layer measurements. For 3D visualization, the volume data are obtained with the combination of reconstructed 2D multi-slices images by FBP method in cosine filter and nearest interpolation. Volume viewer application in MATLAB provided for different views for the volumetric images with different orientations [6]. 3D voxel images of fan beam by MATLAB with different orientations are shown in figure 8.

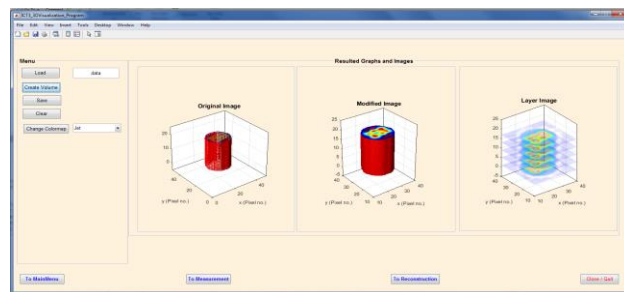


Figure 8. The Interface of GCTS Visualization Program

4.5 Experimental Procedure

For the measurement with the Lab-scaled fan-beam gamma CT system firstly need to check the electronic system and control system. In this system, the scanning object material was set up to be able to scan rotational and translational movements on sample rotator between the source and detector mounting system.

For the measurement the research sample is placed on sample rotator between source and detector. After that the GCTS measurement program was opened and checked the connection to hardware. And then set the initial parameters for measurement and started the measurement for require projections.

During the measurement the object can be rotated 360° around to be scanned and also can be translated to scan cross-sections at any axial position of the source-detector. After the completion of the measurement along with arc translation positions, the object is rotated as sample rotator to the angular position to acquire the next set of measurements. The detector record the

intensity of each step of transmission in 10 second counting time and display the sum of measured intensity in the interface program.

After getting the complete measurement, GCTS measurement program the intensity profile data was saved into default output file with (*.mat) extension, which can be used to reconstruct and analyze the measured data.

5. Results and Discussion

5.1 Results on Design for Fan-Beam Gamma CT

For the field application in industrial field we have been designed single-source and single-detector fan-beam Gamma Computed Tomographic Scan (GCTS) system and tested the Lab-scaled experimental design of GCTS system is constructed in Nuclear Physics Laboratory, Department of Nuclear Physics at D.S.A. The measurement of lab-scaled industrial computed tomography system for the proposed experimental design with arc geometry in good agreement with the simulation result by using MCNP4C.

5.2 Results on of Lab-scaled Fan-Beam Gamma CT System

The Lab-scaled Gamma-ray CT Scanning system is constructed in Nuclear Physics Laboratory, Department of Nuclear Physics at D.S.A. This system is the new lab-scaled design of the third generation of Industrial Computed Tomography system based on gamma transmission method and the fan-beam geometry of single-source and single-detector scanning system. In this system measurements can be performed with scanning object in different density materials by using different gamma radiation sources. According to the results, mechanical motion system of sample and detector is required 16x64 minimum of projection to generate images depending on measurement condition.

5.3 Results on Image Reconstruction and Visualization

The image reconstruction and measurement program GCTS was also created by MATLAB with image processing and analysis tools. In the 2D image reconstruction program are produced the images by BP and FBP methods with interpolation functions. After reconstruction this program produces the reconstructed image with adding different effects and colourmaps can also be applied to improve the resolution of images. The comparison of reconstructed images for research sample with FBP method and optical camera image in GCTS Program and Result images of 2D images and 3D volumetric visualization are shown in figure 9.

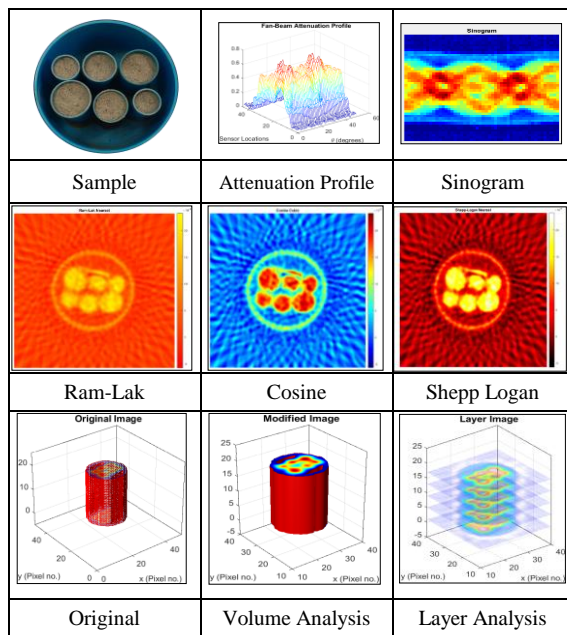


Figure 9. 2D and 3D Volume Results Images

The reconstructed images of industrial object with 32x128 projection is enough to determine the cross sectional images of an object. From the reconstructed images with different projections in fan-beam geometry, the greater number of projections produces the higher resolution images. By using image reconstruction GCTS program images from FBP method with cosine filter and nearest-interpolation produce good resolution images comparing with others filters and interpolation. According to the 3D visualization result, we can be analyzed the structure of researched sample object. The image reconstruction and visualization by MATLAB improves the resolutions of images that distinguish clearly high and low density materials in fan-beam geometry and can be determined the physical parameters of the object by using with special functions of image processing toolbox.

5.4 Discussion on Results

According to the results of measurement and simulation for 3rd generation lab-scaled industrial computed tomography system, the proposed experimental design for fan beam measurement system with arc geometry can be designed for industrial application.

By the resulted images with different projections this system has been needed to develop the measurement system with high performance motion control to produce the higher resolution images.

From the reconstructed images with different projections in fan-beam geometry by using GCTS program, the greater number of projections produces the higher resolution images for 2D and 3D structural analysis.

According to the reconstructed images obtained from current lab-scaled fan-beam CT system with traditional fan-beam system with multi-detectors and parallel-beam

system, current fan-beam CT based on single-source and single-detector system can also produce the clear and good resolution images.

6. Conclusion

In the current research work, we have been designed the new experimental design of fan-beam gamma CT with single-source and single-detector system for analysis and application of industrial fields.

According to the results of constructed lab-scaled experimental setup and simulation of GCTS system we improve that the proposed experimental design can be distinguish different density materials and can be analyzed the external and internal structures of sample object.

The future plans of current research work are to develop the mechanical system of lab-scaled CT system and to construct the experimental compact portable fan-beam gamma CT system based on single-source and single-detector system for industrial field applications.

7. Acknowledgement

The current research work was carried out at the Department of Nuclear Physics, D.S.A. and the authors gratefully acknowledge to respective persons at Nuclear Physics Department, D.S.A. for providing experimental facilities for this research work.

8. References

- [1] Avinash C. K, Malcolm S. Principles of Computerized Tomographic Imaging, IEEE PRESS, 1999.
- [2] IAEA-TECDOC 1589, “Industrial Process Tomography, final report of a coordinated research project 2003-2007, International Atomic Energy Agency”, Austria, 2008.
- [3] “Introduction to Computed Tomography”, General Electric Co., 1976.
- [4] R. Gholipour-Peyvandi, S.Z. Islami-Rad* and M. Ghannadi-Maragheh, “Influence of Gamma Energy in the Image Contrast for Material with Different Density”, International Journal of Pure and Applied Physics, Volume 6, pp. 447–454, No. 4, 2010.
- [5] “MATLAB Image Processing Tool Manual”, Volume 1 & 2.
- [6] “MATLAB 3D Visualization Manual”, 2015.
- [7] “MATLAB GUI Manual”, 2015.

Investigation of Range-Energy Relation In Nuclear Emulsions

Mar Mar Htay¹, Khin Swe Myint²

Physics Department^{1,2},

Myanmar Institute of Information Technology¹, Mandalay University²

[Mar Mar Htay@miit.edu.mm](mailto:Mar.Mar.Htay@miit.edu.mm)¹

Abstract

We calculated the kinetic energies of various particles for different tracks in nuclear emulsion from range-energy relation derived from a simplified model. In our research work, firstly we studied collision between charged particles, energy loss by collision, stopping power and range-energy relation. This relation consists of the number of atoms, the average atomic number and the density of emulsion plate. We solved numerically the range-energy formulation to obtain the kinetic energy of particles for various tracks in emulsion plates. The kinetic energies of particles which decay in emulsion from Fuji ET 7D emulsion plates used in E373 experiment for five tracks were determined from range-energy relation. Our result values for various particles, namely, p, d, t, ^3He , ^4He , ^3H , ^4H , ^4He , ^5He and ^6He are compared with above experimental data of Lambda hypernuclei in nuclear emulsion. It is found that there are some discrepancies between the results which is mainly due to simplification imposed in our formalism.

Keywords: range, energy, nuclear emulsion, hyper nuclei

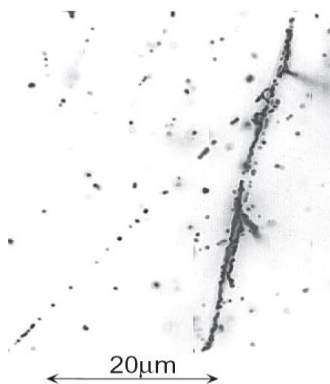
1. Introduction

An emulsion stack consisted of eleven or twelve plates with $24.5 \times 25.0 - \text{cm}^2$ area. Since the most upstream plate was used to connect Ξ^- -hyperon tracks from the SciFi-Bundle detector, it was necessary to minimize the distortion of the emulsion gel of the plate. For this reason, a thin emulsion plate was located upstream followed by ten or eleven thick emulsion plates [1]. The thin plate had 70- μm -thick or 100- μm -thick emulsion gel on both sides of a 200- μm -thick plastic base film, and each thick plate had 500- μm -thick emulsion gel on both sides of a 40- μm -thick or 50- μm -thick plastic film.

All emulsion plates were prepared in Gifu University with the following procedure. First emulsion gel was poured to one side of the plastic films. They were dried in a drying cabinet which moved emulsion plates automatically so that they were dried uniformly. After drying the emulsion gel, gel was poured to the other side of the plates and dried in the same manner. Then, the emulsion plates were dried again with lower humidity. Each of the emulsion plates

was divided to four plates with the size of $24.5 \times 25.0\text{cm}^2$.

(a) Top view



(b) Side view

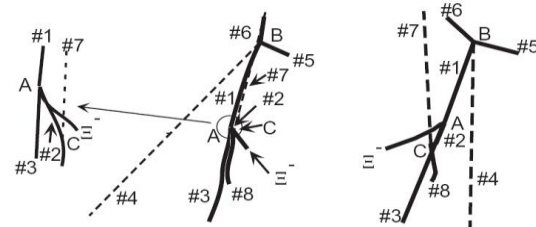
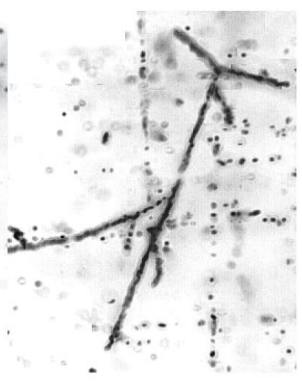


Figure 1. Picture and Schematic Drawing of the Event Viewed from the Vertical (a) and the Horizontal (b) Direction [2].

Figure 1. shows a picture and a schematic drawing of the event from E373 experiment [2]. The purpose of this experiment is to study double-strangeness nuclei produced via Ξ^- hyperon capture at rest. The Ξ^- was captured by a nucleus at point A. Three charged particles (track #1, #2, #3) were emitted from point A. Track #1 shows the topology of a decay into three charged particles at point B. Track #2 also shows a topology of decay into two charged particles at point C.

Table (1) summarizes the ranges and the emission angle of these tracks. The ranges were measured prior to swelling the emulsion. A package "SRIM 2000" [3,4,5] was used to calculate a kinetic energy from a range. The density of the emulsion of this plate was determined as $3.5 \pm 0.07\text{g/cm}^3$ deduced from the measurement of the weight and volume of the emulsion plates. The two ranges at two different energies well with the range-energy relation calculated with SRIM2000.

Table 1. Ranges and Emission Angles of the Tracks [2].

	Track	Range(μm)	Θ(degree)	Φ(degree)
Point A	#1	19.1±0.4	113±7	262±7
	#2	5.2±0.5	66±7	97±8
	#3	23.0±0.4	66±3	78±2
Point B	#4	12517	87.14±1.2	48.19±1.2
	#5	286±4	150±1.0	153.1±1.2
	#6	7.7±0.6	40±4	265±4
point C	#7	≥14884	88±1.5	257.1±0.7
	#8	8.8±0.4	77±5	81±3

2. Formulation of Range and Energy Relation

We consider collision between charged particles of mass M_1 , charge ze , and the velocity v_1 approach a stationary particle of mass M_2 and charge Ze . If the force between particles at distance r is given by the law of inverse square.

$$F = \frac{zZe^2}{4\pi\epsilon_0 r^2} \quad (1)$$

The impulse due to the Coulomb force is

$$\int_0^\infty \frac{zZe^2}{4\pi\epsilon_0 r^2} \cos \psi dt = \int_{-\infty}^\infty \frac{zZe^2}{4\pi\epsilon_0 r^2} \cos \psi \frac{ds}{v}. \quad (2)$$

By substituting equation (1) in equation (2) and we obtain,

$$\Delta q = \frac{zZe^2}{4\pi\epsilon_0} \int_{-\frac{\pi}{2}}^{\frac{\pi}{2}} \frac{\cos \psi d\psi}{pv_1}. \quad (4)$$

$$\Delta q = \frac{zZe^2}{2\pi\epsilon_0 pv_1} \cos \frac{\theta}{2}. \quad (5)$$

According to equation (5),

$$2M_1 v_1 \sin \frac{\theta}{2} = \frac{zZe^2}{2\pi\epsilon_0 pv_1} \cos \frac{\theta}{2} \quad (6)$$

and then, obtained the impact parameter as

$$p = \frac{zZe^2}{4\pi\epsilon_0 M_1 v_1^2} \frac{\cos \frac{\theta}{2}}{\sin \frac{\theta}{2}}. \quad (7)$$

$$p = \frac{b}{2} \cot \frac{\theta}{2} \quad (8)$$

where, $b = \frac{zZe^2}{2\pi\epsilon_0 M_1 v_1^2}$. b is the collision

diameter.

The corresponding energy loss of the incident heavy particle is

$$Q = \frac{1}{2} \frac{(\Delta q)^2}{m} = \frac{z^2 e^4}{8\pi^2 \epsilon_0^2 m p^2 v^2}. \quad (9)$$

As the heavy particle passes through a thickness of absorber in which there are N atoms of atomic number Z per m^3 the number of collisions transferring energy between Q and $Q+dQ$ is the number of electrons within

the annulus of area $2\pi p dp$. The total energy transferred, for all impact parameters,

$$dT = 2\pi NZ dx \int_{P_{\min}}^{P_{\max}} Q pdp \quad (10)$$

$$\frac{dT}{dx} = \frac{NZ}{4\pi\epsilon_0^2} \frac{z^2 e^4}{mv^2} \log \frac{P_{\max}}{P_{\min}} \quad (11)$$

For $P_{\min}=0$, the energy loss becomes infinite.

Where m is the electron mass and Q_0 is the maximum energy transferred which can be seen

$$Q_0 = 2mv^2 = \frac{4m}{M} T \quad (12)$$

with $T=1/2 Mv^2$ the initial kinetic energy of the heavy particle.

$$dT = \pi NZ dx Q_0 \frac{b^2}{4} \log \frac{P_{\max}^2 + \frac{b^2}{4}}{P_{\min}^2 + \frac{b^2}{4}} \quad (13)$$

$$\text{Here, } Q_0 = 2mv^2 \text{ and } b = \frac{ze^2}{2\pi\epsilon_0 mv^2}.$$

The stopping power of charged particle by matter is as follow. The stopping power is defined as the energy lost by the particle per unit path in the substance. The theory of the stopping power depends on knowledge of the behavior of electrons in atoms. If the range is known as the function of energy, the stopping power can be written as,

$$\frac{dT}{dx} = NZ \frac{z^2 e^4}{8\pi\epsilon_0^2 mv^2} \log \frac{P_{\max}^2 + \frac{b^2}{4}}{P_{\min}^2 + \frac{b^2}{4}} \quad (14)$$

In this P_{\min} may be set equal to 0, corresponding with the energy transfer Q_0 . We thus put $P_{\max} = \frac{v}{\omega}$.

Assuming that $P_{\max} \gg b/2$, the stopping power formula becomes

$$\frac{dT}{dx} = \frac{NZ}{8\pi\epsilon_0^2} \frac{z^2 e^4}{mv^2} \log \frac{4P_{\max}^2}{b^2}. \quad (15)$$

To a good approximation,

$$\frac{dT}{dx} = \frac{z^2 e^4}{4\pi\epsilon_0^2 mv^2} NZ \log \frac{2mv^2}{I} \quad (16)$$

$$\text{where, } I = \frac{\omega ze^2}{2\pi\epsilon_0 v}.$$

Finally, we obtained the stopping power as above equation (16).

The range of a heavy charged particle is equal to its path length in matter because the scattering is negligible. The stopping power varies with the energy of particle, and the range of the particle is given by

$$R = \int_0^T \frac{dT}{dx} \quad (17)$$

The range may formally be obtained by integration of the expression for energy loss and the log term is neglected.

$$R = \int_0^T \frac{8\pi e_0^2 m}{z^2 e^4 NZM} T dT \quad (18)$$

We obtained range and energy relation as the following equation,

$$R = \frac{4\pi e_0^2 m}{z^2 e^4 NZM} T^2. \quad (19)$$

We also calculated range-energy relation by including log term as follow.

$$R = \int_0^T \frac{4\pi e_0^2 m v^2}{z^2 e^4 NZ} \frac{1}{\log(2mv^2/I)} dT \quad (20)$$

$$R = \frac{8\pi e_0^2 m}{z^2 e^4 NZM} \int_0^T \frac{T}{\log\left(\frac{4mT}{MI}\right)} dT \quad (21)$$

This formulation consists of the number of atoms, the average atomic number and the density of emulsion plate. The density of Fuji ET 7D emulsion is 3.55×10^{-39} g/fm³. This formulation consists of the number of atoms, the average atomic number and the density of emulsion plate. The density of Fuji ET 7D emulsion is 3.55×10^{-39} g/fm³. Table (2) shows the composition of the Fuji ET-7C and ET-7D emulsion [6]. We calculated the total atoms and average mass number of Fuji ET 7D emulsion. The average atomic number of emulsion is obtained 34.553 by summing the atomic number of each element by considering the weight ratio in emulsion plate. The total atoms of emulsion plate is obtained from Avogadro's law.

The lengths of tracks (Ranges) are used in E-373 experiment [2]. We solved numerically equation (19) and (21) by using FORTRAN code to obtain the kinetic energies of various particles for various ranges in emulsion plate.

Table 2. The Composition of the Fuji ET-7C and ET-7D Emulsion [6].

material	weight ratio(%)	mol ratio(%)
I	0.3	0.06
Ag	45.4	11.2
Br	33.4	11.1
S	0.2	0.2
O	6.8	11.3
N	3.1	5.9
C	9.3	20.6
H	1.5	40.0

3. Results and Discussion

We calculated the average atomic number (Z) and the total number of atoms of emulsion plate by considering the weight ratio of each element in the emulsion. The density of Fuji ET 7D emulsion is 3.55

$\times 10^{-39}$ g/fm³. The lengths of tracks which we used in emulsion plate from E-373 experiment [2]. We solved numerically equation (19) and (21) to obtain the kinetic energies of various particles by using the simplified model. The results are shown in tables (3), (4) and (5).

Ichikawa et, al calculated the kinetic energies of possible particles for various tracks from range-energy relation which contains emission angle of the tracks (θ and ϕ) by using a package 'SRIM 2000' [2]. Their acceptable particles are 4He for track #6 and #3, proton for track #5 and 5He for track #1 and #2. They assumed that Ξ^- hyperon was absorbed by light nucleus ${}^{14}N$ in the emulsion. Their results are shown in the following tables.

We calculated the kinetic energies of possible particles (p, d, t, 3He , 4He) for three tracks(track #6, #3,#5). The results are shown in table (3) and (4). It is seen that our results which neglect log term, agree fairly with the results of Ichikawa et, al [2] for short range but do not agree for long range. Our results which contain log term agree fairly with the results of Ichikawa et, al [2] for long range but do not agree for short range. Our calculated kinetic energy of acceptable particle (4He) for track #6 and #3 which neglect log term, agree with the results of Ichikawa et, al [2].

The kinetic energies of hyper-nuclei (${}^3{}_A H$, ${}^4{}_A H$, ${}^4{}_A He$, ${}^5{}_A He$, ${}^6{}_A He$) for track #1 and #2 were calculated from equation (19) and (21). The results are shown in table (5). It is observed that our result is in better agreement with those of Ichikawa et, al [2] for the longer the tracks. Our result which contains log term for ${}^5{}_A He$ is in agreement with those of Ichikawa et, al [2] for track #1 and #2. This particle is acceptable particle.

Table 3. Various Kinetic Energies of Possible Particles for Track #6 (7.7 μm), Track #3 (23 μm) with our Results A , B and Ref [2].

Particles	Kinetic energy (MeV)			Kinetic energy (MeV)		
	A	B	track #6 [2]	A	B	track #3 [2]
p	0.610	0.550	0.67	1.029	1.168	1.39
d	0.801	0.610	0.79	1.455	1.272	1.74
t	0.981	2.468	0.84	1.781	3.080	1.96
3He	2.122	1.585	2.2	3.563	3.959	4.80
4He	2.350	1.645	2.3	4.104	4.200	5.33

Table 4. Various Kinetic Energies of Possible Particles for Track #5(286 μm) with our Results A, B and Ref [2].

Particles	Kinetic energy (MeV)		
	A	B	track #2[2]
p	3.625	6.160	6.62
d	5.120	7.945	8.7
t	6.272	9.987	10.2
^3He	12.543	21.790	23.5
^4He	14.451	24.355	26.4

Table 5. Various Kinetic Energies of Possible Particles for Track #2 (5.2 μm) and by Track #1 (19.1 μm) with our Results A, B and Ref [2].

Particles	Kinetic energy (MeV)			Kinetic energy (MeV)		
	(A)	(B)	Track #2 [2]	(A)	(B)	track #1 [2]
$^3\Lambda\text{H}$	0.824	0.590	0.58	1.678	0.641	1.75
$^4\Lambda\text{H}$	0.943	0.825	0.56	1.882	1.615	1.88
$^4\Lambda\text{He}$	1.887	2.150	1.6	3.843	4.500	4.73
$^5\Lambda\text{He}$	2.096	1.625	1.6	4.270	4.900	4.98
$^6\Lambda\text{He}$	2.290	1.888	1.6	4.666	4.680	5.18

4. Conclusion

We calculated the kinetic energies of various particles (p, d, t, ^3He , ^4He , $^3\Lambda\text{H}$, $^4\Lambda\text{H}$, $^4\Lambda\text{He}$, $^5\Lambda\text{He}$, $^6\Lambda\text{He}$) for various tracks from range-energy relation by using a simplified model. Ichikawa et, al calculated the kinetic energies of various particles (p, d, t, ^3He , ^4He , $^3\Lambda\text{H}$, $^4\Lambda\text{H}$, $^4\Lambda\text{He}$, $^5\Lambda\text{He}$, $^6\Lambda\text{He}$) whose tracks are found in Fuji ET 7D emulsion from E373 experiment [2]. They obtained the kinetic energy of various particles by using a package "SRIM 2000". They assumed that target as ^{14}N which absorbed Ξ^- at rest and they take the emission angles (θ, ϕ) which are shown in table (1.1).

We calculated the kinetic energies of various particles (p, d, t, ^3He , ^4He). It is observed that our calculated results which neglect log term, agree fairly with the results of Ichikawa et, al [2] for short range but do not agree for long range. Our calculated results which contain log term, agree fairly with the results of Ichikawa et, al [2] for long range but do not agree for short range.

We also calculated the kinetic energies of hyper-nuclei ($^3\Lambda\text{H}$, $^4\Lambda\text{H}$, $^4\Lambda\text{He}$, $^5\Lambda\text{He}$, $^6\Lambda\text{He}$) for two tracks. Our result is in better agreement with those of Ichikawa et, al [2] for the longer the tracks. It is found that there are some discrepancies between the results which is mainly due to assumptions imposed in our formalism. The assumptions, made in our model are as follows, (i) collision is a forward direction ($\theta = 0$, $\phi = 0$) (ii) $P_{\max} \gg b/2$, where P_{\max} = impact parameter, b =collision diameter (iii) $I = kZ$, where $k = 11.5\text{eV}$ (I' is deduced from experimental results) (iv) the atomic number and mass number of target is the average atomic number and mass number emulsion plate.

5. Acknowledgement

We would like to thank Theoretical Nuclear Physics Group in Mandalay University for their valuable discussion and advice during the research work.

6. References

- [1] H. Akikawa *et al.*, to be submitted to Nucl. Instrum . Meth. A. "The BaBar detector", Nucl.Instrum.Meth. A479, ,INSPIRE, Japan (2013) pp 615-701
- [2] A. Ichikawa *et al.* "Experimental study of double-Lambda hypernuclei with nuclear emulsion" Phys. Lett. B 500, Japan (2001) pp 37-46.
- [3] J. F. Ziegler, J.P. Biersack, Srim-2000, <http://www.research.ibm.com/ionbeams/home.htm>.
- [4] J. F. Ziegler, J.P. Biersack, U. Littmark, "The Stopping and Range of Ions in Matter" Springer, Boston, MA, 1985.
- [5] J.P. Biersack, L.G. Haggmark, "A Monte Carlo computer program for the transport of energetic ions in amorphous targets", Nucl. Methods 174 ,Elsevier B.V., (1980) pp 257-269.
- [6] H. Takahashi, (thesis) "Study of Double-Hypernuclei with Hybrid-Emulsion Method", Kyoto University, Japan(2003)

Relativistic Ground State Energy of Deeply Bound Kaonic Nuclear System K^- - ^{208}Pb

Thida Wint¹, Kyi Kyi Win², Khin Swe Myint³

Associate Professor¹, Associate Professor², Emeritus Professor³

Department of Physics^{1,2,3}

Mandalay University of Distance Education¹, Taunggyi University², University of Mandalay³

thidarwint@gmail.com¹, kyikyiwin@gmail.com², profkhinswemyint@gmail.com³

Abstract

In this research, relativistic ground state energy of K^- - ^{208}Pb nuclear system are calculated by solving the Klein-Gordon equation. In addition, non-relativistic ground state energy of that nuclear system is calculated as well by solving the Schrödinger equation to investigate the relativistic correction for deeply bound nuclear system. Woods-Saxon potential is used for the interaction between anti-kaon and ^{208}Pb nucleus. In the case of relativistic calculation, the nuclear potentials are considered to be scalar as well as vector type. The significance of relativistic effect on deeply bound kaonic nuclear system is investigated by changing the Woods-saxon potential depth. From the calculated results of our investigation, it is concluded that relativistic effect on deeply bound nuclear system is more pronounced in large potential depth.

Keywords- relativistic Klein-Gordon equation, Woods-Saxon potential depth, deeply bound kaonic nuclear system

1. Introduction

Kaonic atom and kaonic nuclei carry important information concerning the antikaon \bar{K} - nucleon interaction in nuclear medium. This information is very important to determine the constraints such as optical potential and equation of states (EOS) on kaon condensation in high density matter. The interaction between the antikaon and nucleon is strong attraction. This indication leads to interesting theoretical prediction i.e. extra-ordinary nuclear states, which are more compact and dense than normal nucleus, could be produced by embedding the antikaon in nucleus as superglue.

Considerable interest in recent years has focused on the question of possible existence of deeply bound K^- -nuclear states, and whether such states are sufficiently narrow to allow experimental identification. Kishimoto [1], Akaishi and Yamazaki [2, 3], suggested to look for K^- -nuclear states bound by over 100 MeV, for which the dominant $\bar{K} N \rightarrow \pi \Sigma$ decay channel would become kinematically forbidden. Furthermore, it was suggested that multi- K^- high-density nuclear clusters should also exist, providing perhaps a precursor

stage to kaon condensation [4]. It was noted that the typical threshold density of kaon condensation in nucleons (only neutron star matter) was about 2-4 ρ_0 , where ρ_0 is normal nuclear matter density [5]. However, the threshold of anti-kaon condensation is sensitive to the anti-kaon optical potential and depends more strongly on the equation of state.

In the year 2000, Baca et al., had studied anti-kaonic nuclear bound state and computed the binding energies and width for both \bar{K} and \bar{K}^0 by using density dependent optical potential. For \bar{K} nuclear clusters, the binding energies of ^{12}C and ^{208}Pb are 153 MeV and 197 MeV respectively. For \bar{K}^0 nuclear clusters, their binding energies are 149 and 173 MeV respectively [6].

In addition, the nuclear ground states of a K^- in 3He , which is K^- ppn, 4He (K^- ppnn) and 8Be (K^- - 8Be) are investigated [4] within the framework of Brueckner-Hartree-Fock theory. The above mentioned ground states are predicted to be discrete states with binding energies of 108, 86 and 113 MeV and the widths are 20, 34 and 38 MeV, respectively [2]. Their investigation causes the attention of experiment at once.

In the exotic nuclear system, the experimental evidences of kaonic nuclei (K^- ppn, K^- pnn) have been obtained at KEK from 4He (K^- stopped, n) and 4He (K^- stopped, p) reactions respectively. According to the experimental result of 4He (K^- stopped, n) K^- ppn carried out by Iwasaki et al., in KEK, the total binding energy and level width of K^- ppn is found to be 173 ± 4 MeV and 30 MeV [7]. Although this result supports a deep $\bar{K}N$ potential proposed by Akaishi et al.,[2], the binding energy of the experimental result is much larger than the theoretical values which is 108 MeV [2].

There are discrepancies among the theoretical value as well as experimental data. Therefore, investigating theoretically the ground state energy of deeply bound nuclear system is an interesting topic. In addition, relativistic correction is necessary to take into account on such a deeply bound $\bar{K} N$. The aim of our research is to investigate the ground state energy and relativistic effect on deeply bound kaonic nuclear system K^- - ^{208}Pb .

2. Relativistic Klein-Gordon Equation

The success of quantum mechanics in the description of the atomic and sub-micro world is very impressive

and overwhelming. Supplementing this theory with special relativity created one of the most accurate physical theories in recent history. An example is quantum electrodynamics; the theory that describes the interaction of charged particles with the electromagnetic radiation at high speed or strong coupling. The relativistic effect must be considered for a particle in a strong potential field, which gives the correction for non-relativistic quantum mechanics.

The Dirac equation and Klein-Gordon (K-G) equation are the most frequently used wave equations for the description of particle dynamics in relativistic quantum mechanics. In relativistic quantum mechanics, one can apply the K-G equation to the treatment of a zero-spin particle and the Dirac equation for spin half particle.

In nuclear and high energy physics, one of the interesting problems is to obtain exact solution of the K-G equation and Dirac equation for pure vector, pure scalar and mixed potentials.

In this research, K-G equation with Coulomb-like vector potential, scalar potential and mixed scalar and vector potential was solved analytically to understand the relativistic effect in kaonic atomic system.

For a charged 'e' particle with mass 'm', moving in an electromagnetic potential $A_\mu = (\phi, \vec{A})$, the K-G equation is obtained by substituting $P_\mu \rightarrow p^\mu - e A^\mu$ in minimal coupling,

$$\begin{aligned} (\hat{P}^\mu - e A^\mu)(\hat{P}_\mu - e A_\mu)\Psi &= m^2 c^2 \Psi \quad (\text{or}) \\ [\partial_\mu \partial^\mu + m^2 + U] \Psi &= 0. \end{aligned}$$

Where, Potential energy;

$$U = ie \frac{\partial}{\partial x^\mu} A^\mu + ie A^\mu \frac{\partial}{\partial x^\mu} - e^2 A^\mu A_\mu.$$

In above equation, the first two terms give the vector potential, U_v and the last term gives the scalar potential U_s which are coupled to energy E and to rest mass respectively in Klein-Gordon equation as follow;

$$(E - U_v)^2 = p^2 c^2 + (mc^2 + U_s)^2 \quad (1)$$

where, $E = \epsilon + mc^2$, E = total energy, ϵ = relativistic binding energy

Eq.(1) is simplified as follow.

$$\begin{aligned} E^2 - 2EU_v + U_v^2 &= p^2 c^2 + (mc^2)^2 + 2mc^2 U_s + U_s^2 \\ (\epsilon + mc^2)^2 - 2(\epsilon + mc^2)U_v + U_v^2 &= p^2 c^2 + (mc^2)^2 + 2mc^2 U_s + U_s^2 \\ \epsilon + \frac{\epsilon^2}{2mc^2} &= \frac{p^2}{2m} + \frac{\epsilon U_v}{mc^2} + U_v + U_s + \frac{U_s^2 - U_v^2}{2mc^2} \end{aligned} \quad (2)$$

From Eq.(2), equivalent potential is defined by

$$U^{eqv}(r) = U_v + U_s + \frac{U_s^2 - U_v^2}{2mc^2} + \frac{\epsilon U_v}{mc^2} \quad (3)$$

Using the equivalent potential, K-G equation which is Schrödinger like equation can be written as follows,

$$\left(-\frac{\hbar^2}{2m} \nabla^2 + U^{eqv}(r) \right) \Psi = \left(\epsilon + \frac{\epsilon^2}{2mc^2} \right) \Psi$$

If $\epsilon + \frac{\epsilon^2}{2mc^2} = \epsilon_s$, K-G equation becomes,

$$\left(-\frac{\hbar^2}{2m} \nabla^2 + U^{eqv}(r) \right) \Psi = \epsilon_s \Psi \quad (4)$$

ϵ_s = non-relativistic binding energy

ϵ = relativistic binding energy

$\epsilon - \epsilon_s$ = relativistic correction

For pure vector potential case, $U_s = 0$ and the equivalent potential is given by

$$\begin{aligned} U^{eqv}(r) &= U_v - \frac{U_v^2}{2mc^2} + \frac{\epsilon^{(i)} U_v}{mc^2} \\ U^{eqv}(r) &= U_v \left(1 + \frac{\epsilon^{(i)}}{mc^2} \right) - \frac{U_v^2}{2mc^2} \\ \epsilon^{(i)} &= i^{\text{th}} \text{ iteration value of } \epsilon_s \end{aligned}$$

For pure scalar potential, it can be assumed that the vector potential $U_v = 0$. From Eq. (3), equivalent potential for scalar potential is,

$$U^{eqv}(r) = U_s + \frac{U_s^2}{2mc^2}$$

K-G equation for radial part is as expressed in Eq. (4),

$$\left\{ -\frac{\hbar^2}{2\mu} \frac{d^2}{dr^2} + \frac{\hbar^2}{2\mu} \frac{l(l+1)}{r^2} + U^{eqv}(r) \right\} u(r) = E u(r) \quad (5)$$

where, $u(r) = r R(r)$.

3. Interaction of K^- - ^{208}Pb Nuclear System

A successful use of kaons in nuclear structure requires the precise knowledge of the interaction mechanism of kaons with nuclei. Since each theoretical model for the kaon-nuclear interaction starts from the free kaon-nucleon interaction and then adds medium corrections in one way or another, a precise knowledge of the free interaction is absolutely essential.

In the meson exchange framework, Jülich group [8] constructed $\bar{K}N$ interaction considering scalar mesons and vector mesons exchange. In this $\bar{K}N$ interaction model, $\bar{K}N$ interaction is strongly attractive due to combined effect of scalar meson (σ -meson) exchange and vector meson (ρ - and ω -meson) exchange, which all add coherently in the relevant channel.

Therefore, in our calculation, scalar type potential and vector type potential are taken into account for $\bar{K}N$ interaction.

We have employed Wood-Saxon form to represent both vector and scalar potential. Woods-Saxon form is as follows:

$$V(r) = \frac{V_0}{1 + \exp\left(\frac{r - R}{a}\right)}$$

where, $V(r)$ = interaction between K^- and the core nucleus

V_0 = depth of Woods-Saxon potential

r = radial distance from the center

R = nuclear radius, a = range parameter

In the Woods-Saxon potential, the parameters we used are $R = r_0 A^{1/3}$, $r_0 = 1.1$ fm and $a = 0.6$ fm.

4. Ground State Energy of Kaonic Nuclear System $K^- - {}^{208}Pb$

In order to investigate the significance of relativistic effect on deeply bound kaonic nuclear system, relativistic and non-relativistic ground state energy of $K^- - {}^{208}Pb$ system are obtained by solving the non-relativistic Schrödinger equation and relativistic Klein-Gordon equation. And, root-mean-square radius of that nuclear system is also obtained.

First, non-relativistic binding energy of $K^- - {}^{208}Pb$ nuclear system is investigated by solving the Schrödinger equation with Gaussian basic wave function.

The Schrödinger Radial Equation (SRE) is

$$\left\{ -\frac{\hbar^2}{2M} \frac{d^2}{dr^2} + \frac{\hbar^2}{2M} \frac{\ell(\ell+1)}{r^2} + V(r) \right\} u(r) = E u(r) \quad (6)$$

where $u(r) = r R_{nl}$ is the reduced radial wave function.

$$u(r) = r^{\ell+1} \sum_{j=1}^N c_j e^{-\left(\frac{r}{b_j}\right)^2} \quad \text{where } b_j \text{'s are the range}$$

parameter and are chosen to be geometric progression as follows.

$$\frac{b_2}{b_1} = \frac{b_3}{b_2} = \frac{b_4}{b_3} = \dots = \text{constant},$$

$$b_{i+1} = \left(\frac{b_N}{b_1} \right)^{1/(N-1)} b_i \quad \text{and } N \text{ is the number of}$$

coefficients and, c_j 's are expansion coefficients.

The Schrödinger equation is written as follow.

$$(H_0 + V) u = E u$$

where, E = energy eigen value, u = eigen vector, H_0 = kinetic energy operator and V = potential energy operator.

Multiplying both sides of the Eq.(6) by $r^{\ell+1} e^{-\left(\frac{r}{b_i}\right)^2}$ from the left and integration through the equation

$$\int r^{\ell+1} e^{-\left(\frac{r}{b_i}\right)^2} \left\{ -\frac{\hbar^2}{2M} \frac{d^2}{dr^2} + \frac{\hbar^2}{2M} \frac{\ell(\ell+1)}{r^2} + V(r) \right\} \sum_j c_j r^{\ell+1} e^{-\left(\frac{r}{b_j}\right)^2} dr = \\ E \int r^{\ell+1} e^{-\left(\frac{r}{b_i}\right)^2} \sum_j c_j r^{\ell+1} e^{-\left(\frac{r}{b_j}\right)^2} dr$$

We can define the above equation as

$$\sum_j [T_{ij} + V_{ij} + V_{ij}] c_j = E \sum_j N_{ij} c_j$$

where T_{ij} is kinetic energy matrix element, N_{ij} is norm matrix element and V_{ij} is the centrifugal potential energy matrix element. H_{ij} is Hamiltonian matrix

element. The N_{ij} , T_{ij} and V_{ij} are analytically solved by using standard integral form as follows.

The norm matrix element,

$$N_{ij} = \int r^{\ell+1} e^{-\left(\frac{r}{b_i}\right)^2} r^{\ell+1} e^{-\left(\frac{r}{b_j}\right)^2} dr$$

The kinetic energy matrix element,

$$T_{ij} = \int r^{\ell+1} e^{-\left(\frac{r}{b_i}\right)^2} \left\{ -\frac{\hbar^2}{2\mu} \frac{d^2}{dr^2} \right\} r^{\ell+1} e^{-\left(\frac{r}{b_j}\right)^2} dr$$

The centrifugal potential energy matrix element,

$$V_{ij} = \int r^{\ell+1} e^{-\left(\frac{r}{b_i}\right)^2} \frac{\ell(\ell+1)}{r^2} r^{\ell+1} e^{-\left(\frac{r}{b_j}\right)^2} dr$$

The potential energy matrix element,

$$V_{ij} = \int r^{\ell+1} e^{-\left(\frac{r}{b_i}\right)^2} V(r) r^{\ell+1} e^{-\left(\frac{r}{b_j}\right)^2} dr$$

The Hamiltonian matrix element,

$$H_{ij} = \int r^{\ell+1} e^{-\left(\frac{r}{b_i}\right)^2} H r^{\ell+1} e^{-\left(\frac{r}{b_j}\right)^2} dr$$

where $H_{ij} = T_{ij} + V_{ij} + V_{ij}$.

The Schrödinger equation in matrix form can be written as follows.

$$[H] [C] = E [N] [C] \quad (7)$$

Equation (7) can be expanded as

$$H_{11} C_1 + H_{12} C_2 + \dots + H_{1N} C_N = E (N_{11} C_1 + N_{12} C_2 + \dots + N_{1N} C_N)$$

$$H_{21} C_1 + H_{22} C_2 + \dots + H_{2N} C_N = E (N_{21} C_1 + N_{22} C_2 + \dots + N_{2N} C_N)$$

$$H_{N1} C_1 + H_{N2} C_2 + \dots + H_{NN} C_N = E (N_{N1} C_1 + N_{N2} C_2 + \dots + N_{NN} C_N), \text{ which are}$$

$$\sum_{i,j=0}^N (H_{ij} - E N_{ij}) C_j = 0.$$

In order to determine the energy eigen value E , we solved the following set of linear equations iteratively.

$$\sum_{i,j=0}^N (H_{ij} - E_0 N_{ij}) C_j^{(k)} = \sum_{i,j=0}^N N_{ij} C_j^{(k-1)}, k = 1, 2, \dots, \ell \quad (8)$$

$$\text{with } E = E_0 + \frac{C_j^{(k-1)}}{C_j^{(k)}}.$$

where E_0 = initial guess value of energy

E = energy eigen value, N = number of coefficients,

C = expansion coefficient, and ℓ = number of iterations.

The convergence of iteration is obtained when the ratio of

$$\frac{C_j^{(k-1)}}{C_j^{(k)}} \text{ becomes constant.}$$

$$\text{i.e., } \frac{C_j^{(k-2)}}{C_j^{(k-1)}} = \frac{C_j^{(k-1)}}{C_j^{(k)}}.$$

And, relativistic ground state energy of $K^- - {}^{208}Pb$ nuclear system is obtained by solving the K-G equation; Eq. (5) with Gaussian basic treatment as mention above.

We have also calculated the root-mean-squared radius for K^- - ^{208}Pb nuclear systems to see the size of the atoms. Root-mean-squared radius is defined by

$$\langle r^2 \rangle = \int \rho(r) r^2 dV$$

$$\text{root-mean-squared radius} = \sqrt{\langle r^2 \rangle}$$

Density distributions for above mentioned systems have been investigated. Density distribution is defined by

$$\rho(r) = \frac{u^*(r)u(r)}{r^2}.$$

5. Results and Discussion

In order to investigate the relativistic effect on binding energies of (K^- - ^{208}Pb) nuclear system, relativistic Klein-Gordon equation was solved by using Woods-Saxon potential as strong interaction. In the case of relativistic calculation, the nuclear potentials are considered to be scalar as well as vector type. Strength parameter V_0 of Woods-Saxon kaon-nucleus potential is arbitrarily changed from $V_0 = -50$ MeV to $V_0 = -300$ MeV.

Non-relativistic and relativistic ground state energies and root-mean-square (rms) radius for K^- - ^{208}Pb nuclear system with various Wood-Saxon potential strengths V_0 are expressed in table (1) and (2). It is found that the relativistic effect increases about 4.11 % binding energy for $V_0 = -50$ MeV and 27.76 % for $V_0 = -300$ MeV in the K^- - ^{208}Pb nuclear system with scalar type potential. For vector type potential, relativistic effect is about 1.73 % increment in binding energy for $V_0 = -50$ MeV and 29.08 % for $V_0 = -300$ MeV.

From these results, the nuclei with high density are found to have large relativistic effect.

In order to know the difference between the scalar type and vector type potential, the comparisons of relativistic and non-relativistic ground state energies and density distributions of above mentioned nuclear system with Wood-Saxon type scalar potential and vector potential are displayed in figure (1), (2), (3) and (4).

From these figures, it is noted that the relativistic effect on scalar type and vector type potential is not different noticeably.

6. Conclusion

In this research, the relativistic and non-relativistic ground state energy of deeply bound nuclear system K^- - ^{208}Pb is calculated by solving Schrödinger equation and Klein-Gordon equation. Energies and rms radii are calculated by changing the potential strength of Woods-Saxon type scalar and vector potential to investigate the role of relativistic effect in deeply bound nuclear system.

It is concluded that relativistic effect is significantly large in deeply bound and compact kaonic nuclear systems while it is negligible in normal densed nuclei. It is important to take into account relativistic correction in studying deeply bound and highly densed nuclear

system such as kaonic nucleus which is investigated in this research.

Table 1. Non-relativistic and Relativistic Ground State Energies for K^- - ^{208}Pb Nuclear System with Various Woods-Saxon Type Scalar Potential Strengths V_0

V_0 (MeV)	rms radius(fm)	$E_{\text{Non-Rel}}$ (MeV)	E_{Rel} (MeV)	ΔE (%) (MeV)
-50	3.781	-38.974	-40.647	1.673 (4.11%)
-100	3.508	-80.119	-87.954	-7.835 (8.91%)
-150	3.393	-116.810	-135.380	18.570 (13.72%)
-200	3.335	-148.750	-182.470	33.720 (18.48%)
-250	3.310	-175.820	-228.870	53.050 (23.18%)
-300	3.309	-198.000	-274.090	76.090 (27.76%)

5

Table 2. Non-relativistic and Relativistic Ground State Energies for K^- - ^{208}Pb Nuclear System with Various Woods-Saxon Type Vector Potential Strengths V_0

V_0 (MeV)	rms radius (fm)	$E_{\text{Non-Rel}}$ (MeV)	E_{Rel} (MeV)	ΔE (%) (MeV)
-50	3.743	-39.622	-41.354	1.732 (4.19%)
-100	3.435	-81.668	-89.844	8.176 (9.10%)
-150	3.282	-119.250	-138.750	19.500 (14.05%)
-200	3.180	-152.400	-188.320	35.920 (19.07%)
-250	3.104	-180.430	-237.620	57.190 (24.07%)
-300	3.044	-203.620	-287.120	83.500 (29.08%)

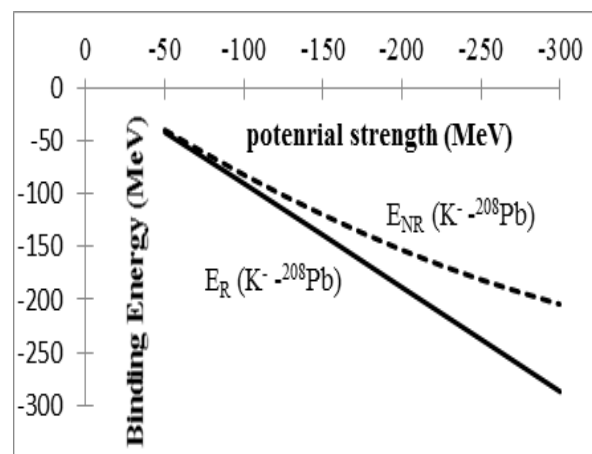


Figure (1) Relativistic and Non-relativistic Energies for K^- - ^{208}Pb Nuclei with Wood-Saxon Type Scalar Potential

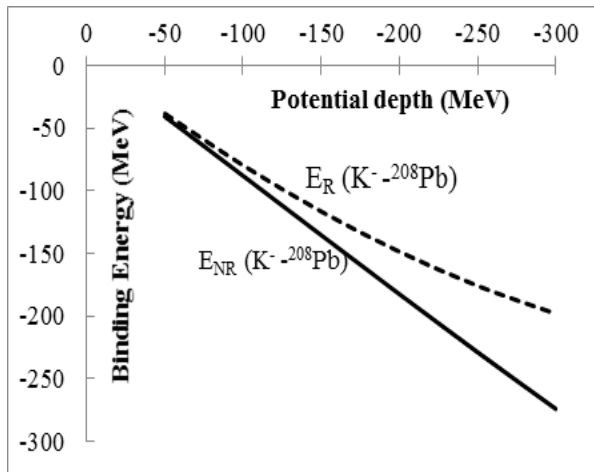


Figure (2) Relativistic and Non-relativistic Energies for $K^- - ^{208}\text{Pb}$ Nuclei with Wood-Saxon Type Vector Potential

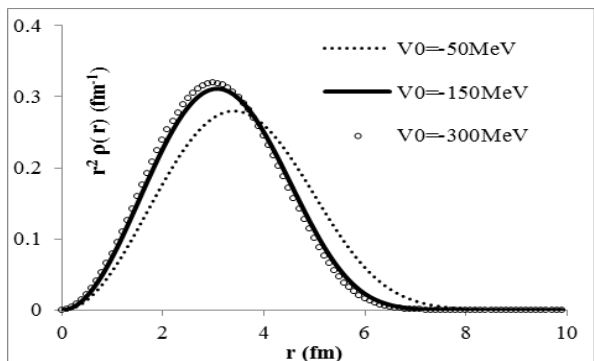


Figure (3) Density Distribution of $K^- - ^{208}\text{Pb}$ Nuclear System with Wood-Saxon Type Scalar Potential for Various Potential Strengths

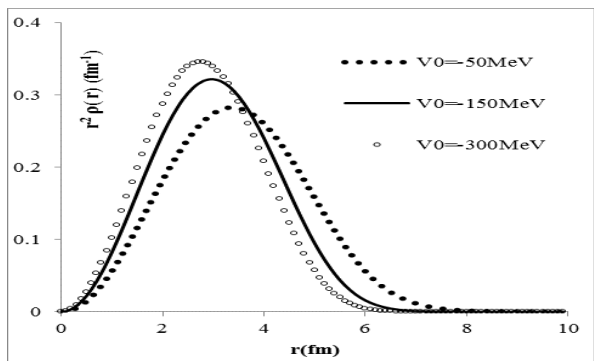


Figure (4) Density Distribution of $K^- - ^{208}\text{Pb}$ Nuclear System with Wood-Saxon Type Vector Potential for Various Potential Strengths

References

- [1] T. Kishimoto, “Kaonic Nuclei Excited by the (\bar{K} , N) Interaction”, Phys. Rev. Lett. **83** (1999) 4701.
- [2] Y. Akaishi and T. Yamazaki, “Nuclear \bar{K} Bound States in Light Nuclei”, Phys. Rev. C **65** (2002) 044005.
- [3] Y. Akaishi and T. Yamazaki, “Overview of \bar{K} -Nuclear Quasi Bound States”, Frascati Physics Series **XVI** (1999) 59.
- [4] T. Yamazaki, A. Doté, and Y. Akaishi, “Invariant-Mass Spectroscopy for Condensed Single- and Double-K Nuclear Clusters to be formed as Residues in Relativistic Heavy-Ion Collisions”, Phys. Lett. B **587** (2004) 167.
- [5] A.E. Nelson, and D.B. Kaplan, “Strange Condensate Realignment in Relativistic heavy ion collisions” Phys. Lett. B **192** (1987) 193.
- [6] A. Baca, C. García-Recio and J. Nieves, “Deeply bound levels in kaonic atoms” Nucl. Phys. A **673** (2000) 335.
- [7] M. Iwasaki *et al.*, “Indication of a Strange Tribaryon S^+ from the ${}^4\text{He}(\text{stopped } K^-,\text{n})$ Reaction”, arXiv:nucl-ex1 (2003) 0310018.
- [8] A. Müller-Groeling, K. Holinde and J. Speth, Nucl. “ \bar{K} N Interaction in the Meson Exchange Framework”, Phys. A **513** (1990) 557.

Theoretical Analysis of Λ -Triton Bound State using One-Range and Two-Range Gaussian Potentials

Kyaw Kyaw Naing

Lecturer

Department of Physics

Defence Services Academy

drkyawkyawnaing4550@gmail.com

Abstract

We have conducted the theoretical analysis of Λ -triton bound state by using two-range Gaussian potential. To solve the bound state between Λ and triton nucleus, the Lippmann-Schwinger equation in momentum space, the Gauss integration method and the iterative method are applied. The kinetic energy, the potential energy and the root-mean-square distance of Λ -triton system are calculated. All the numerical calculations are conducted with the help of Fortran 90 program. It is found that the binding energy and the root-mean square distance values of Λ -triton system for eight kinds of Gaussian type potential are consistent with the experimental value. Among the potentials used in this work, Sine-Gordan (one-range) and Isle (two-range) potentials give the binding energy closest to the experimental value.

Keywords- Gauss integration method, iterative method, triton, Sine-Gordan, Isle

1. Aim

The aim of this paper is to understand the hypernuclear system between Λ particle and triton nucleus and to compare the results of the hypernuclear system between Λ particle and triton nucleus with the theoretical and experimental values.

2. Introduction

Hyperons are unstable elementary particles. There are several types of hyperons. They are Lambda (Λ), Sigma (Σ), Xi (Ξ) and Omega (Ω). Lambda (Λ) hyperon consists of one strange quark and 20% greater than the mass of the nucleon. Lambda (Λ) hyperon is the lightest particle in the family of hyperons; it can stay in contact with nucleons inside nuclei and form hypernuclei [2]. It has a rest energy of 1115 MeV with a lifetime of 2.67×10^{-10} seconds, zero charge, spin (J) = $1/2$, isospin (I) = zero, strangeness (S) = -1, mass is about 1115 MeV/c² and make up of one up, one down and one strangeness. The Λ -hyperon is unstable and is produced in strong interaction but they decay in weak interaction because their lifetime is longer than 2.67×10^{-10} seconds. The decay process conserved neither of strangeness, isospin and parity. A free Λ -hyperon decays almost totally into a pion and a

nucleon. The Λ hyperon was discovered in 1947 by Rochester and Butler using a triggered cloud chamber. A neutral particle was formed in the interaction of cosmic rays in a lead plate and this decay to two oppositely charge particles producing a V-shaped track in photographs [4]. This particle was given the name Λ .

3. One-range and Two-range Gaussian Potentials

The one-range Gaussian potential type is

$$V(r) = V_0 e^{-\left(\frac{r}{b}\right)^2} \quad (1)$$

where,

V_0 = potential depth parameter

b = range parameter

r = distance between two particles

The two-range Gaussian potential type is

$$V(r) = V_R e^{\left(-\frac{r^2}{b_R^2}\right)} - V_A e^{\left(-\frac{r^2}{b_A^2}\right)} \quad (2)$$

where,

V_R = potential depth parameter for repulsive part

V_A = potential depth parameter for attractive part

b_R = range parameter for repulsive part

b_A = range parameter for attractive part

4. Calculation of Binding Energy for Λ -Triton System

If someone calculates the binding energy for Λ -triton system, they will construct the wave function for this system. This wave function determines some physical phenomena in this area. So we initiate the time independent Schrödinger equation.

$$\hat{H} |\Psi\rangle = E |\Psi\rangle \quad (3)$$

\hat{H} is the total energy hamiltonian and E is the energy eigenvalue. The Lippmann-Schwinger equation in momentum space is

$$|\Psi\rangle = \frac{1}{E - \hat{H}_0} \hat{V} |\Psi\rangle \quad (4)$$

\hat{H}_0 is kinetic energy operator and \hat{V} is potential energy operator. So equation (4) becomes

$$|\Psi\rangle = \frac{1}{E - \frac{\hat{p}^2}{2\mu}} \hat{V} |\Psi\rangle \quad (5)$$

where, μ is the reduced mass. By using partial wave analysis, the wave function for Λ -triton system is

$$\Psi_\ell(p) = \frac{1}{E - \frac{\hat{p}^2}{2\mu}} \int p'^2 dp' V_\ell(p, p') \Psi_\ell(p') \quad (6)$$

where, $V_\ell(p, p')$ is the potential matrix element. When solving the above equation in integral form, it is too long and too many steps to satisfy. Therefore we solved this equation into summation form by using Gauss integration method.

$$\Psi(p_i) = \frac{1}{E - \frac{\hat{p}_i^2}{2\mu}} \sum_{j=1}^{N_p} p_j^2 W_j V(p_i, p_j) \Psi(p_j) \quad (7)$$

where, p_j and W_j are Gauss point and Gauss weight and N_p is the number of the grid point.

By using one-range and two-range Gaussian potentials, the wave function for Λ -triton system is obtained.

5. Calculation of Kinetic Energy and Potential Energy for Λ -Triton System

To obtain the kinetic energy and potential energy for Λ -triton system, the normalized condition is used.

$$\int p^2 dp \Psi^*(p) \Psi(p) = 1 \quad (8)$$

The condition for normalized and unnormalized wave function is

$$\Psi_{nol}(p) = \frac{1}{\sqrt{\int p^2 dp \Psi_{un}^*(p) \Psi_{un}(p)}} \Psi_{unol}(p) \quad (9)$$

The kinetic energy and the potential energy for Λ -triton system is

$$K.E = \frac{1}{2\mu} \int p^4 dp \Psi^*(p) \Psi(p) \quad (10)$$

$$P.E = \int p^2 dp \int p'^2 dp' \Psi^*(p) V(p, p') \Psi(p') \quad (11)$$

6. Calculation of Root-mean-square Distance for Λ -Triton System

To find the root-mean-square distance between particle Λ and triton, the wave function must be transformed momentum space into configuration space.

$$\Psi_l(r) = \sqrt{\frac{2}{\pi}} \int p^2 dp i^l j_l(pr) \Psi_{lm}(p) \quad (12)$$

For the particular case, $\ell = 0$ and using the spherical bessel function $j_0(pr) = \frac{\sin(pr)}{pr}$ and therefore

$$\Psi(r) = \sqrt{\frac{2}{\pi}} \int p dp \sin(pr) \Psi(p) \quad (13)$$

The average mean square distance between the particle Λ and triton is

$$\langle r^2 \rangle = \int \Psi^*(r) r^2 \Psi(r) dr \quad (14)$$

Then, the root-mean square distance between the particle Λ and triton is

$$r_{rms} = \sqrt{\frac{\langle r^2 \rangle}{2}} \quad (15)$$

7. Results and Discussion

The values of binding energy, kinetic energy, potential energy and the root-mean-square distance of Λ -triton system are calculated. The parameters sets for various Λ -triton potentials [1] such as Tang Herndon (TH), Gibberellin (Gib), Sine-Gordan (SG), Dalitz-Down (DD), Isle, Dalitz, Deloff and Maria Sutrop Alkeda (MSA) are shown in table (1).

Table 1. Parameter Sets for Eight Kinds of Gaussian Potential

Types of Potential	V_A (MeV)	V_R (MeV)	b_A (fm)	b_R (fm)
Tang Herndon (TH)	-60.17	-	1.273	-
Gibberellin(Gib)	-43.48	-	1.576 4	-
Sine-Gordan (SG)	-37.12	-	1.7	-
Dalitz-Down (DD)	-43.93	-	1.566	-
Isle	-78.07	95.86	1.7	1.12
Dalitz	-404.88	450.43	1.41	1.25
Deloff	-143.42	148.58	1.368	1.05
Maria Sutrop Alkeda (MSA)	-95.0	91.0	1.70	1.30

Now we are going to observe the numerical stability of computer program to study the binding energy for Isle (two-range) Gaussian potential.

At the first step, we put the initial point of momentum $p_0 = 0.0 \text{ fm}^{-1}$, the mid-point of momentum $p_{mid} = 5.0 \text{ fm}^{-1}$ and the maximum point of momentum $p_{max} = 10.0 \text{ fm}^{-1}$ in our program. Then we study the value of binding energy by varying the number of grid point (N_p). These results are expressed in table 2. According to table 2, we have found that the value of binding energy is converged at the number of grid point $N_p = 37$.

At the second step, we fix the initial point of momentum $p_0 = 0.0 \text{ fm}^{-1}$ and $p_{mid} = 10.0 \text{ fm}^{-1}$. We increase the maximum value of $p_{max} = 20.0 \text{ fm}^{-1}$. We observe that the binding energy is converged at the

number of grid point $N_p = 53$ which is shown in table 3.

Table 2. Convergence of Binding Energy (BE) by Changing the Number of Grid Point N_p for $p_{max}=10 \text{ fm}^{-1}$

p_0	p_{mid}	p_{max}	N_p	B.E(MeV)
0.0	5.0	10.0	19	2.039409
0.0	5.0	10.0	21	2.038143
0.0	5.0	10.0	23	2.038595
0.0	5.0	10.0	25	2.038977
0.0	5.0	10.0	27	2.039079
0.0	5.0	10.0	29	2.039068
0.0	5.0	10.0	31	2.039048
0.0	5.0	10.0	33	2.039041
0.0	5.0	10.0	35	2.039041
0.0	5.0	10.0	37	2.039042
0.0	5.0	10.0	39	2.039042
0.0	5.0	10.0	41	2.039042

Table 3. Convergence of Binding Energy (BE) by Changing the Number of Grid Point N_p for $p_{max}=20 \text{ fm}^{-1}$

p_0	p_{mid}	p_{max}	N_p	B.E(MeV)
0.0	10	20	41	2.039070
0.0	10	20	43	2.039054
0.0	10	20	45	2.039044
0.0	10	20	47	2.039041
0.0	10	20	49	2.039041
0.0	10	20	51	2.039041
0.0	10	20	53	2.039042
0.0	10	20	55	2.039042
0.0	10	20	57	2.039042
0.0	10	20	59	2.039042
0.0	10	20	61	2.039042
0.0	10	20	63	2.039042

At the third step, we increase the maximum value of $p_{max} = 30.0 \text{ fm}^{-1}$. Then we study the value of binding energy by varying the number of grid point (N_p). We have found that the value of binding energy is converged at the number of grid point $N_p = 65$ which is shown in table 4.

At the fourth step, we increase the maximum value of $p_{max} = 40.0 \text{ fm}^{-1}$. Then we study the value of binding energy by varying the number of grid point (N_p). We have found that the value of binding energy is converged at the number of grid point $N_p = 75$ which is shown in table 5. Finally, we choose that the stable binding energy is $E = 2.039042 \text{ MeV}$. This is the theoretical results of the binding energy for Λ -triton system.

Table 4. Convergence of Binding Energy (BE) by Changing the Number of Grid Point N_p for $p_{max}=30 \text{ fm}^{-1}$

p_0	p_{mid}	p_{max}	N_p	B.E(MeV)
0.0	15.0	30.0	55	2.039045
0.0	15.0	30.0	57	2.039041
0.0	15.0	30.0	59	2.039041
0.0	15.0	30.0	61	2.039041
0.0	15.0	30.0	63	2.039041
0.0	15.0	30.0	65	2.039042
0.0	15.0	30.0	67	2.039042
0.0	15.0	30.0	69	2.039042
0.0	15.0	30.0	71	2.039042
0.0	15.0	30.0	73	2.039042
0.0	15.0	30.0	75	2.039042
0.0	15.0	30.0	79	2.039042

Table 5. Convergence of Binding Energy (BE) by Changing the Number of Grid Point N_p for $p_{max}=40 \text{ fm}^{-1}$

p_0	p_{mid}	p_{max}	N_p	B.E(MeV)
0.0	20.0	40.0	75	2.039042
0.0	20.0	40.0	77	2.039042
0.0	20.0	40.0	79	2.039042
0.0	20.0	40.0	81	2.039042
0.0	20.0	40.0	83	2.039042
0.0	20.0	40.0	85	2.039042
0.0	20.0	40.0	87	2.039042
0.0	20.0	40.0	89	2.039042
0.0	20.0	40.0	91	2.039042
0.0	20.0	40.0	93	2.039042
0.0	20.0	40.0	95	2.039042
0.0	20.0	40.0	97	2.039042

The comparison of the theoretical results and experimental results of binding energy, kinetic energy,

potential energy and root-mean square distance of Λ -triton system for various Gaussians potential are shown in table 6.

Table 6 The Results of Kinetic Energy, Potential Energy, Binding Energy and Root-mean Square Distance for Λ -triton System

Potential Types	KE (MeV)	PE (MeV)	BE (MeV)	RMS (fm)
Experimental Results	-	-	2.04±0.04 [3]	2.0±0.2 [3]
Tang Herdon (one-range)	10.121434	-12.388831	2.267396	1.5107
Gibberellin (one-range)	8.434559	-10.683533	2.248974	1.5450
Sine-Gordan (one-range)	7.140667	-9.179961	2.039294	1.6814
Dalitz-Down (one-range)	8.492815	-10.642107	2.149292	1.5421
Isle (two-range)	5.290808	-7.329851	2.039042	1.8257
Dalitz (two-range)	6.102355	-8.442139	2.339784	1.6882
Deloff (two-range)	7.272473	-9.518473	2.246000	1.5906
Maria Sutrop Alkeda (two-range)	6.068566	-8.248412	2.179846	1.6645

The behavior of Tang Herdon potential for one-range attractive part in configuration space is shown in figure 1. In this figure, the potential is gradually increased within the range from 0 fm to 1.9 fm, again gradually increased within the range from 1.9 fm to 2.7 fm. And then the potential is stationary beyond the range 2.7 fm and above. Moreover the behavior of Tang Herndon potential for one-range attractive part in momentum space is shown in figure 2.

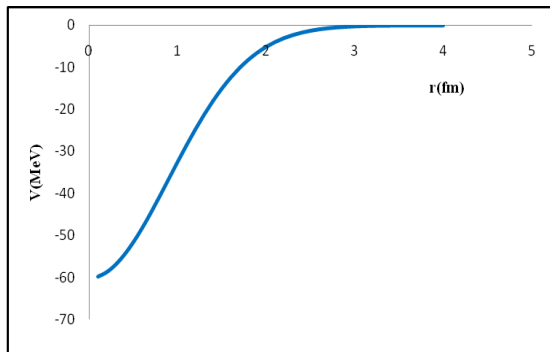


Figure 1. One-range Tang Herdon Potential in Configuration Space

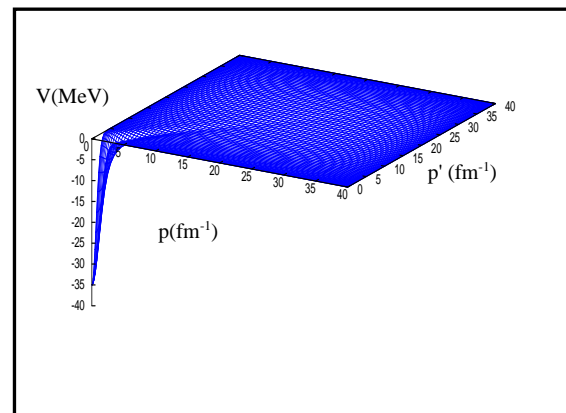


Figure 2. One-range Tang Herdon Potential in Momentum Space

The behavior of Gibberellin potential for one-range attractive part in configuration space is shown in figure 3. In this figure, the potential is gradually increased within the range from 0 fm to 3.5 fm. And then the potential is stationary beyond the range 3.5 fm and above. Moreover the behavior of Gibberellin potential for one-range attractive part in momentum space is shown in figure 4.

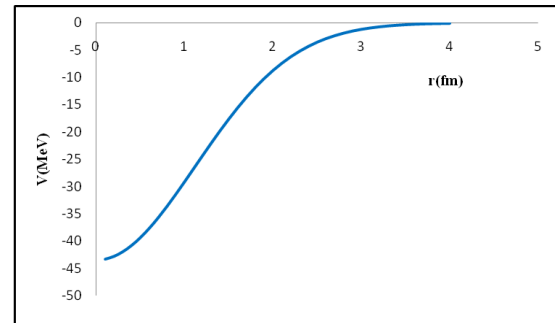


Figure 3. One-range Gibberellin Potential in Configuration Space

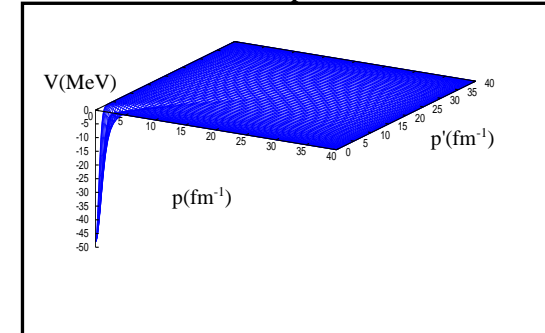


Figure 4. One-range Gibberellin Potential in Momentum Space

The behavior of Sine-Gordan potential for one-range attractive part in configuration space is shown in figure 5. In this figure, the potential is gradually increased within the range from 0 fm to 3.5 fm. And then the potential is stationary beyond the range 3.5 fm and above. Moreover the behavior of Sine-Gordan potential for one-range attractive part in momentum space is shown in figure 6.

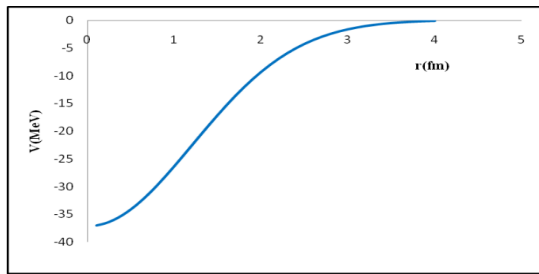


Figure 5. One-range Sine-Gordan Potential in Configuration Space

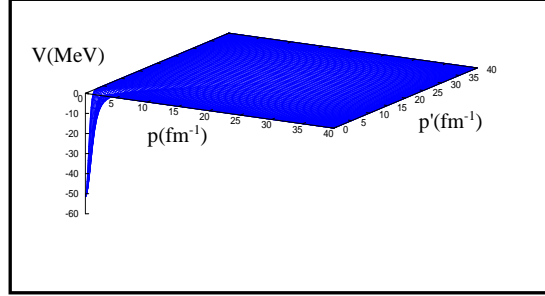


Figure 6. One-range Sine-Gordan Potential in Momentum Space

The behavior of Dalitz-Down potential for one-range attractive part in configuration space is shown in figure 7. In this figure, the potential is gradually increased within the range from 0 fm to 3.5 fm. And then the potential is stationary beyond the range 3.5 fm and above. Moreover the behavior of Gibberellin potential for one-range attractive part in momentum space is shown in figure 8. The behavior of two-range gaussian type Isle potential in configuration space is shown in figure 9. In this figure, the potential is rapidly decreased within the range from 0 fm to 1.5 fm. But the potential is gradually increased within the range from 1.5 fm to 3.5 fm. And then the potential is stationary beyond the range 3.5 fm and above. Moreover the behavior of two-range gaussian type Isle potential in momentum space is shown in figure 10.

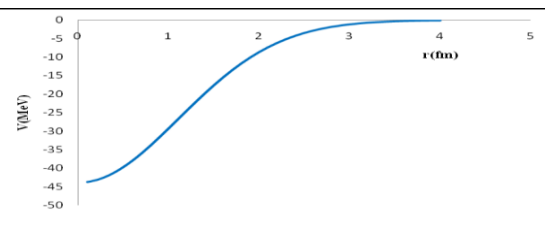


Figure 7. One-range Sine-Gordan Potential in Configuration Space

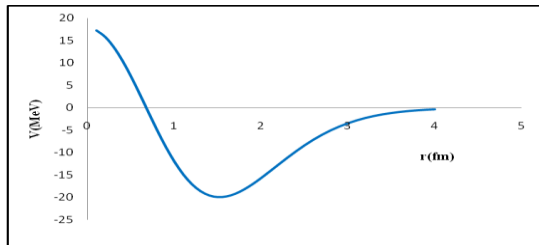


Figure 8. One-range Sine-Gordan Potential in Momentum Space

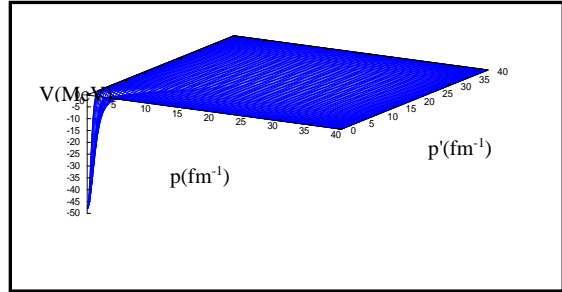


Figure 9. Two-range Isle Potential in Configuration Space

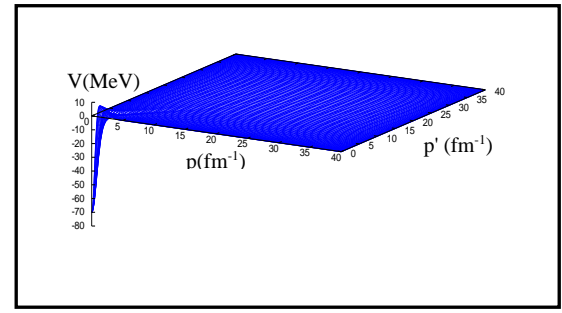


Figure 10. Two-range Isle Potential in Momentum Space

The behavior of two-range gaussian type Dalitz potential in configuration space is shown in figure 11. In this figure, the potential is rapidly decreased within the range from 0 fm to 1.6 fm. But the potential is gradually increased within the range from 1.6 fm to 3.6 fm. And then the potential is stationary beyond the range 3.6 fm and above.

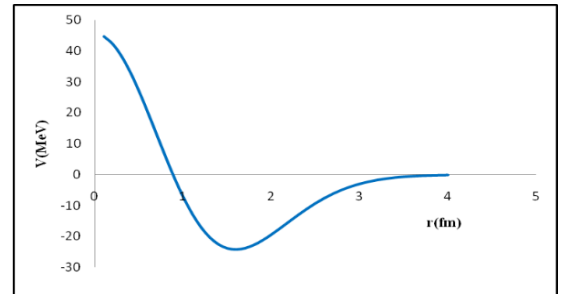


Figure 11. Two-range Dalitz Potential in Configuration Space

Moreover the behavior of two-range gaussian type Dalitz potential in momentum space is shown in figure 12.

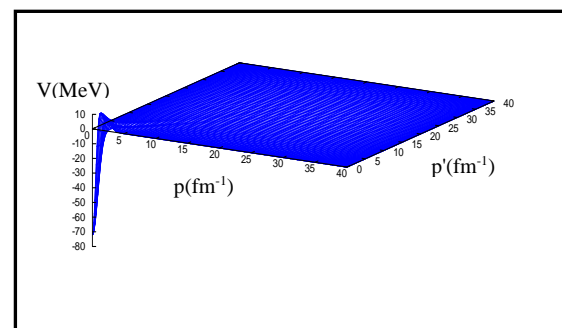


Figure 12. Two-range Dalitz Potential in Momentum Space

The behavior of two-range gaussian type Deloff potential in configuration space is shown in figure 13. In this figure, the potential is rapidly decreased within the range from 0 fm to 1.3 fm. But the potential is rapidly increased within the range from 1.3 fm to 2.6 fm, again gradually increased within the range from 2.6 fm to 3.5 fm. And then the potential is stationary beyond the range 3.5 fm and above. Moreover the behavior of two-range gaussian type Deloff potential in momentum space is shown in figure 14.

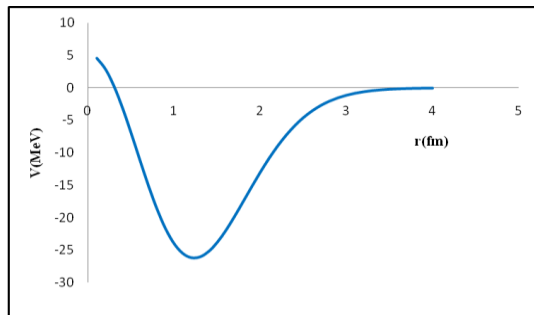


Figure 13. Two-range Deloff Potential in Configuration Space

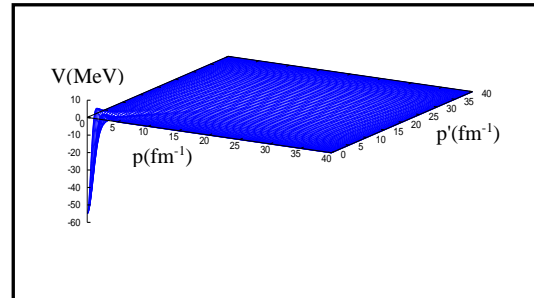


Figure 14. Two-range Deloff Potential in Momentum Space

The behavior of two-range gaussian type MSA potential in configuration space is shown in figure 15. In this figure, the potential is rapidly decreased within the range from 0 fm to 1.5 fm. But the potential is rapidly increased within the range from 1.5 fm to 4 fm. And then the potential is stationary beyond the range 4 fm and above. Moreover the behavior of two-range gaussian type MSA potential in momentum space is shown in figure 16.

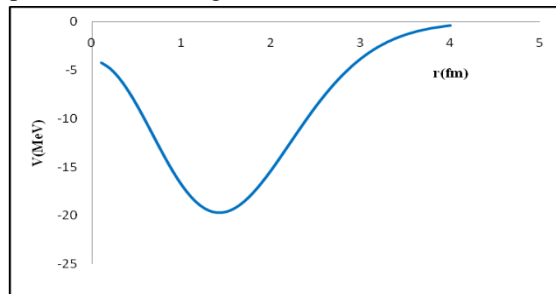


Figure 15. Two-range MSA Potential in Configuration Space

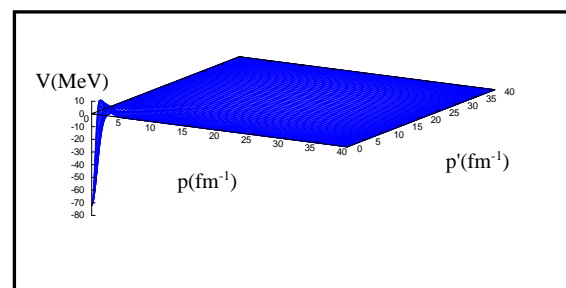


Figure 16. Two-range MSA Potential in Momentum Space

8. Conclusion

The values of binding energy obtained from the theoretical calculation for one-range Gaussian potential are 2.267396 MeV for Tang Herdon, 2.248974 MeV for Gibberellin, 2.039294 MeV for Sine-Gordan and 2.149292 MeV for Dalitz-Down. Moreover, the value of binding energy obtained from the theoretical calculation for two-range Gaussian potential are 2.039042 MeV for Isle, 2.339784 MeV for Dalitz, 2.246000 MeV for Deloff and 2.179846 MeV for MSA. Since the experimental value of binding energy for Λ -triton system is 2.04 ± 0.04 MeV. So, it can be found that Sine-Gordan and Isle potentials give the binding energy closest to the experiment value.

9. References

- [1] Y. Akaishi and S. Okabe, “Evidence for a Central Repulsion Potential from Pionic Decay of S-shell Λ -hypernuclei”, Hokkaido University, Japan, **369** (2002).
- [2] A. Fessahatsion., “Cluster model of S and P-shell $\Lambda\Lambda$ Hypernuclei”, Ababa University, Ethiopia, **68** (2007).
- [3] H. Tamura and S. R. Hayano., “Study of Λ -Hypernuclei with Stopped K Reaction”, University of Tokyo, Japan, **133** (2004).
- [4] M. Nakazawa and H. Kamada., “Few-Body System”, Gifu University, Japan, **129** (2000).

Applications of Monte Carlo Simulation MCNP for Gamma Computed Tomography CT Scanning

Kyaw Lin Oo¹, Khaing Nyunt Myaing², Zin Bo Oo³, Myo Zaw Htut⁴, Kyaw Htay Naing⁵

Department of Nuclear Physics^{1,3,4,5}, Department of Nuclear Technology²

D.S.A^{1,3,4,5}, Technological University (Kyaukse)²

kyawlinoo53@gmail.com¹, khaing.nm@gmail.com², mzhtut@gmail.com³,

bolay.ru@gmail.com⁴, kyawhtaynaing@gmail.com⁵

Abstract

Industrial nuclear imaging technique such as gamma computed tomography CT scanning is able to analyze and identify failures point inside the pipe vessel, permitting to visualize internal structure. The aim of current research work is applications of Monte Carlo N-Particle Transport Code MCNP simulations for gamma CT scanning system in the inspection of pipe vessel for future development of system design. The CT scanning system consist of ^{60}Co gamma source strength of 2.5 mCi and NaI(Tl) scintillation detector with 5mm aperture lead collimator for source and detector were used. In the present study, lab scaled column containing the steel rod assembly was used for structural inspection by CT scanning measurements and MCNP simulations. Image reconstruction results from Monte Carlo simulation showed that the tomographic system provided the good image solution for industrial objects. MCNP simulation provided the preliminary data for the CT scanner, which will be used for system developement in the future work.

Keywords-gamma computed tomography, image reconstruction, MCNP simulations,

1. Introduction

Gamma Computed tomography (CT) is a tool for revealing the internal structural of components non-destructively. CT requires many projections to be acquired from different view angles after which a suitable image reconstruction algorithm is adopted for reconstruction. CT technique used penetration radiation (e.g. X-rays, neutrons, and gamma rays) throughout the object from different angular views and acquires projections from each view. The contrast of tomography image in projections depends on the changes in radiation intensity due to attenuation in the object. The attenuation coefficient is a quantity that measures how easily a radiation beam can absorb or scatter across the material it encounters on its passage [1].

Radiation imaging is a non-invasive imaging technique which produces an image due to the variation of the transmitted radiation intensity through the object. The radiation intensity varies due to attenuation caused by different structures in the object with varying thickness, density or atomic composition [2].

An image reconstruction algorithm based on radon transform functions maps the attenuation coefficients and generates a cross-sectional image of the object from the acquired projections. In the present study the cross sectional reconstructions produced 2D cross sectional images of an object and developed to generate a three-dimensional (3D) reconstruction of the object which was implemented in the MATLAB graphical user interface GUI [3].

The aim of current research work is applications of Monte Carlo N-Particle Transport Code MCNP simulations for modelling of the gamma CT scanning system for inspection of pipe vessel in the visualization of internal structure and development of tomography CT scanner for the future experimental work.

2. Material and Methods

Gamma computed tomography CT scanning can generate a 2D cross-section of an object from multiple projections. The mathematics algorithms used to obtaining the cross sectional image is called the CT reconstruction. Tomography CT scan starting from data acquisition, the entire process is categorized into two major steps: one is the data acquisition and the other is the data reconstruction. The reconstructions from parallel beam provide the 2D cross section of a slice. With the advent of 2D detectors and faster computers, 3D reconstruction is developed using image reconstruction in MATLAB.

For the generation of virtual experimental data for gamma computed tomography CT imaging MCNP 4C code was used in the current research work. MCNP stand for Monte Carlo N-Particle transport code. The MCNP is one of the most extensively used Monte Carlo simulation codes in the nuclear industry. The technique has been well established as a research and application tool in nuclear industries. This code has been used for nuclear medicine, nuclear safeguard, accelerator, homeland security, nuclear criticality, dose assessments, shield calculations, radiation measurements and in nuclear industries. It can simulate the transporting and interaction of radiation with matters. There is a growing interest in the Monte Carlo simulation code in radiation technology as well as nuclear reactor technology. In this paper, the details procedure of tomography CT scanning

by MCNP simulation and the results of reconstructed images are presented.

2.1 Principle of Computed Tomography

In transmission imaging, quantity of interest is the spatial distribution of the linear attenuation coefficient, $\mu(x,y)$ which is necessary for attenuation compensation in single photon computed tomography. CT cross-section of an object is produced by reconstructing transmission data using an image reconstruction algorithm. The data is obtained by measuring the attenuation of photons along a large number of lines through the cross-section from different angles. For each angle, a set of measurement data for a full translation of the source-detector/object is called a projection. Before applying any of the reconstructing algorithms, the projection data p is processed as:

$$p_j = \ln(I_{0j}/I_j) \quad (1)$$

Where I_{0j} and I_j are the counts recorded by detector at position j of the acquired data taken with and without the object, respectively [2].

2.2 Image Reconstruction Program GCTS

Image reconstruction program “GCTS” was used to generate the images, which was related to the density distribution of object based on gamma-ray attenuation in research objects. The image reconstruction program firstly loads the measured intensity profile (energy spectrum file) which was saved by measurement program. And then program initialized the data and created intensity profile, projection data and sinogram data. These projection data was used in the simple back projection (BP) and filtered back projection (FBP) methods based on Radon and inverse Radon transforms functions for image reconstructions. The main interface of GCTS image reconstruction program indicating the 2D and 3D image reconstruction is shown in Figure 1.



Figure 1. Interface of 2D and 3D Image Reconstruction by GCTS Program in MATLAB

In the current research work image reconstruction was carried out by implemented program GCTS in MATLAB Graphic User Interface GUI. The images are reconstructed from the projections by the back projection method (BP) and filter back-projection (FBP) with different filtering and interpolation functions were used in order to improve the resolution of images and determination of the influence on the reconstructed

image. the interface of 2D image reconstruction by GCTS program in MATLAB showing projection, sonogram and 2D reconstructed image is indicated in Figure 2.

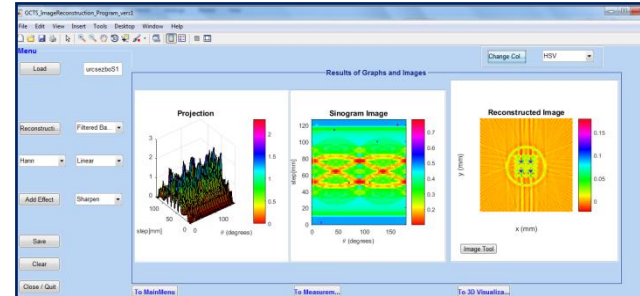


Figure 2 Interface of 2D Image Reconstruction by GCTS Program in MATLAB

2.2.1 Development of 3D visualization program. In the present research work, the development of the image reconstruction from 2D to 3D image visualization was implemented by using with image processing and visualization tools in MATLAB package. In the development of 3D image visualization program, the 3D volume data was created from multi-slices 2D reconstructed image data from CT measurements of researched samples.

In this program the image with different color map can be changed by clicking “Change Colormap Button” and different color map can be chosen. In addition special image effects such as sharpen, emboss and edge effect can be applied by the use of image processing tool in GCTS program. This program also improves the resolutions of images that distinguish clearly high and low density materials inside the pipe vessel.

Image reconstruction of 3D volumetric image was performed by clicking “Create Volume”. After construction 3D program displays the 3D voxel image with different transparencies and multi-slices image in axes of program interface. Interface for image 3D visualization program is illustrated in program includes three main axes. First axis area was used for creating volumetric image and second axis area was used to change transparency and the third axis area was used to check slice by slice using counter slice function. The 3D visualization of reconstructed images in GCTS image reconstruction program interface with 3D volume image and layer image is shown in Figure 3.

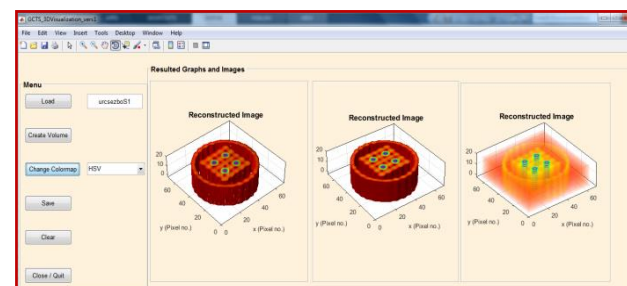


Figure 3. Interface of 3D Image Reconstruction by GCTS Program in MATLAB

3. MCNP Simulations for Gamma Computed Tomography

Monte Carlo simulation setup MCNP [5] is one of the most commonly used radiation transport codes for simulation of tomographic data. Simulations were performed for same the geometry of experimental work with parallel beam measurement system. To generate tomographic data, transmitted radiation from 64×64 projections per view of measuring points is calculated. The source and detector rotates 2.8° angle with 64 steps for 180° and moved translational through 4.9mm total effective length of 317 mm. Projections for the sample pipe column PVC with 21cm diameter with steel tube assembly of 5×5 array with steel tubes with air hole and solid steel rods were calculated. The radiation source is simulated as a gamma source, which is a ^{60}Co in capsule of 5 mm diameter 7.5mm length and 33 mm cylindrical active volume. The cladding of source is 1.5mm thick and made of stainless steel. The source capsule is contained in lead collimator. The function of collimator is to confine the beam direction to face the detector. The source collimator has cylindrical tungsten shielding block with 5mm windows with lead collimator. The detector model is NaI(Tl) scintillation crystals with 2.54 cm × 2.54 cm active area and 2.0cm depth. Figure 4(left) shows the geometry of source with lead collimator, and the right side indicated the NaI(Tl) scintillation detector with lead collimator. The sample to be canned for simulation is steel tube assembly placed inside the pipe column. In this sample contain PVC pipe containing the 21 steel tubes with 4 solid steel rods assembly of same sizes. The geometry specification of sample is indicated in Figure 5 top view in left and front view in the right.

MCNP4C is used to generate virtual experimental data for gamma computed tomography for structural inspection of pipe column. Pulse height spectra from F8 tally of MCNP are obtained for single channel counting data of photo-peak and gross counting. Photo-peak and gross counting data are reconstructed for the cross-sectional image of simulation of pipe column sample with steel tube assembly by back projection BP, filter back projection FBP with different filter functions by implemented image reconstruction program GCTS (gamma computed tomography system) program in MATLAB. The data collection program was implemented in MATLAB for collection of gamma tomographic data for image reconstruction from the results of MCNP simulation.

3.1 Implementations of Input File for CT Scanning

The input files for gamma computed tomography CT scanning are created that is subsequently read by MCNP. This input file contains information about the geometry specification, the description of materials and

selection of cross-section evaluations, the location and characteristics of photon, the type of answers or tallies desired.

The MCNP input file describes the problem geometry, specifies the materials and the source, and defines the results desired from the calculation. The geometry is constructed by defining cells that are bounded by one or more surfaces. Cells can be filled with a material or be void. An MCNP input file has three major sections: cell cards, surface cards, and data cards. A one-line title card precedes the cell card section. A section consists of one or more cards [5].

3.1.1 MCNP simulation setup. In input card, the 1x1 inch scintillation detector coated with aluminum window is cell number 52 and 53, and the detector collimator which has lead shielding block with 1 cm hole in the center is cell number 54 and 55 shown in figure 4(left). The ^{60}Co source coated with stainless steel capsule is cell number 58 and 59, and the source collimator which has lead shielding block with 1 cm hole in the center is cell number 61 and 62 shown in figure 4. (right). Geometry of sample used in CT scan is shown in Figure 5 with top and side view.

3.1.2 Definition of material specification. One of the important definitions is material specification by considering atomic number, mass number, and density for object materials. The material information used to calculate the CT scan is indicated in the Table 1.

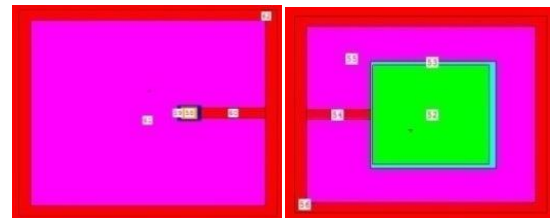


Figure 4. Geometry of Source and Detector with Lead Collimator

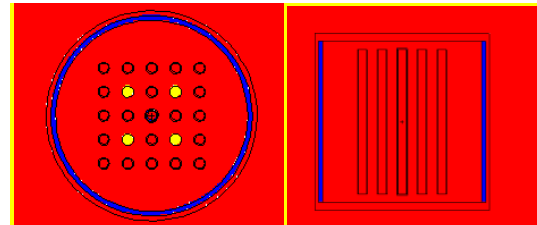


Figure 5. Geometry of Sample to be Scanned Top View and Front View

Table 1 Material Information for Monte Carlo Simulation

Material	Chemical form	Density (g/cm ³)	Size (cm) (diameter)
Scintillator	NaI	3.6	2.54
Co-60	Co	8.9	0.37
Stainless Steel	Fe, Ni,Cr	7.9	0.65
PVC	(CH ₂ CH ₃ Cl) _n	1.41	21.0
Lead	Pb	11.34	4.5

3.1.3 Definition of tally specification. For the simulation of each, 10^7 photons are generated from the

source. The detector response function was determined by means of pulse-height tally named F8 tally in the MCNP input file. This tally scores the energy distribution of pulses created in a detector by radiation. The net response was the spectra of pulses with heights proportional to the frequency of events in distinct energy bins. The energy bins are set 0 to 1 MeV. The MCNP-4C Monte Carlo computer code provides a special data treatment suitable for pulse high distribution data acquisition, which is the Gaussian energy broadening (GEB) (card FTn) option. It is used to fit the full energy peak shape of the pulse high distribution to a Gaussian response of an experimental measurement. The GEB parameters, as an input for the MCNP-4C code, have been set taking into account the resolution of the detector. These geometry are chosen for same conditions in the experimental measurements.

C*****Tally Card

```
F8:P (35<47)
E8 0 99I 1.5
FT8 GEB 0 0.08922 -0.15373
PRDMP J J 1 J J
nps 1e7
```

3.3 Preparation and Running in MCNP

The execution file, cross-sectional library file, input file and Visual Editor for geometrical and material checking are located in a folder. To run MCNP with different file names, type mcnp inp= and then the file name of the example problem followed by outp= and the name of the output file. After making an input file according to MCNP format, it should be checked whether the geometry and materials are true or not graphically using the Visual Editor as shown in figure 6. The process of running MCNP was used command prompt. MCNP writes information to the screen about how the calculation is progressing. After completing the calculation can be checked the output file to see results. The run time for this problem should be on the order of minutes or less.

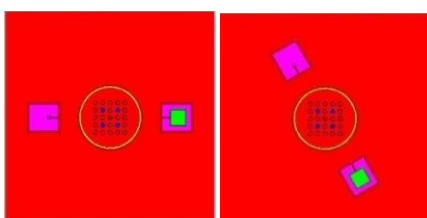


Figure 6. Geometry of Gamma CT Scanning by MCNP Simulation with Different Source Detector Position

3.3.1 Gamma column scanning by MCNP simulation. In this section, MCNP simulation was calculated virtual experimental data for gamma-ray column imaging system. In this simulation, single source-single detector gamma-ray imaging technique which consist of 1x1 inch scintillation detector NaI(Tl) and ^{60}Co gamma source was used. To generate tomographic data, repeated structure cards in MCNP such as Universe, TRCL, LIKE BUT, FILL CARD and

coordinated transformation card TR for projection and transmission of sample vessel were used. A series of input files with different rotation angle and steps of column are calculated and result data from output files are collected in load MCNP program and generated reconstructed images by the use of MATLAB program.

3.3.2 Definition of coordinate transformation card TR.

The coordinate transformation card (TR) was used for rotation and translation of research column as a method of define an auxiliary Cartesian coordinate system. Accordingly, the parameters specified in the definition of each coordinate transformation can be interpreted either as the translation vector and the rotation angles applied to the original cell, equivalently, as the position of the origin and the directions of the axes of auxiliary coordinate system. Each coordinate transformation is defined using the following format:

*TRn O1O2 O3 B1B2B3B4B5B6B7B8B9 M

Where n is the number of the transformation: $1 < n < 999$.

*TRn means that Bi are angles in degrees rather than being the cosines of the angles. O1 O2 O3 are displacement vector of the transformation and B1 to B9 are rotation vector of the transformation. M = 1 mean that the displacement vector is the location of the origin of the auxiliary coordinate system, defined in the main system and M = -1 mean that the displacement vector is the location of the main coordinate system, defined in the auxiliary system.

In the present work, the projections are obtained by 64 steps and 64 views for 180 degree and defining the coordinate transformation for scan column in X Y plane by 2.8 degree from origin is as following:

```
c o1 o2 o3 xx' yx' zx' xy' yy' zy' xz' yz' zz' m
*tr1 0 0 0 0.0 90 90 90 0.0 90 90 90 0 1
*tr2 0 0 0 0.0 90 90 90 0.0 90 90 90 0 1
*tr3 0 0 0 0.0 90 90 90 0.0 90 90 90 0 1
```

3.4. Overall Procedure for Gamma CT Scanning by MCNP Simulation

The first step is to preparing input files which are used for making a series of input files. If all the MCNP input files are created, following steps are needed to carry out MCNP calculation by batch file in DOS prompt window. After calculation is completed, the Mctal, Output and Runtpc files are generated and developed in MATLAB program GCTS for data processing sub program. MCNP output files was collected and arranged the data from output files to a format suitable for image reconstruction. The overall procedure for the gamma-ray CT scanning by MCNP simulation is shown in figure 7.

There is a significant amount of information contained in the output file, which are echo of input file, some tables, particle history summaries, tally results with energy bins and errors, and overall tally summary. Tally results with energy bins were collected from output file generated by MCNP and then the data is collected by implemented program in MATLAB graphical user interface GUI.

For running the input files of 64 by 64 projections for scanning position, 4096 input files were prepared and made a batch file to run in dos prompt window. After completing the calculation, output files generated by MCNP simulation were collected and arranged to a suitable format for image reconstruction by MATLAB GCTS Program as indicated in figure 7.

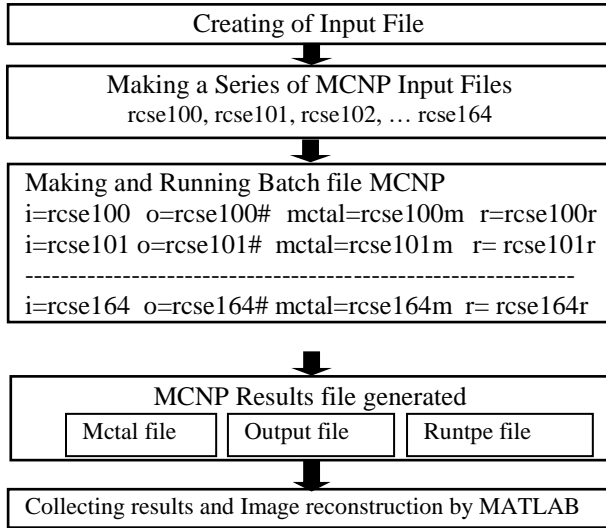


Figure 7. Implementation Steps for the Gamma CT Scanning by MCNP Simulations

4. Results and Discussion

The results of 2D cross sectional images of gamma CT scanning of pipe column by MCNP simulations is indicated in the Figure 8. The results of 2D images are reconstructed by GCTS image reconstruction program implemented in MATLAB with back projection method BP and filter back projection method FBP with different filter functions. According the results the image indicates the clear graphical representation of high and low density inside the PVC pipe clearly. These 2D reconstructed data are used to produce 3D images by creating the layer images in MATLAB. The results of 3D images with different orientations and layers of 3D images is indicated in Figure 9. The 3D volume image obtained by MCNP simulation in comparison with experimental results and optical camera image of inspected pipe column is shown in Figure 10.

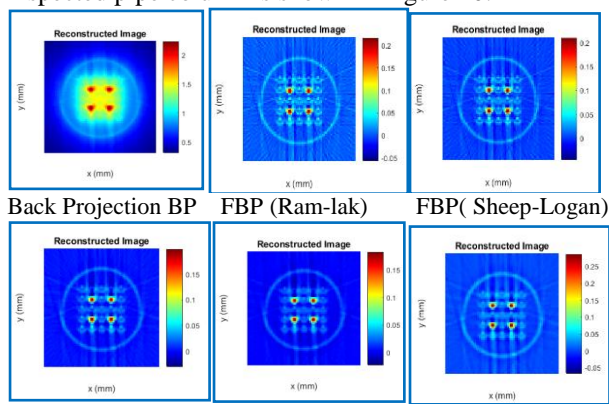


Figure 8. The Results of 2D Cross Sectional Images with BP and FBP Method with Different Filter Functions

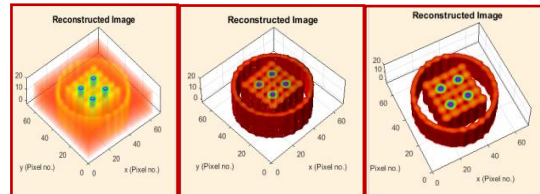


Figure 9. Results of 3D Layer Image and Volume Images with Different Orientation

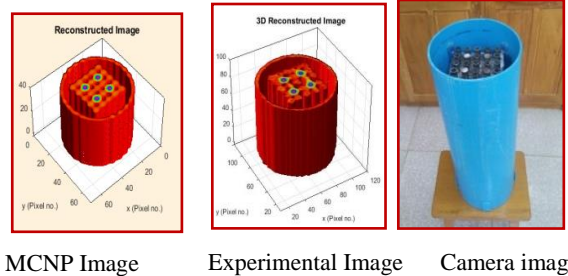


Figure 10. MCNP Results of 3D Volume Images in Comparison with Experimental Results and Camera Image

3D volume image of gamma CT scanning by MCNP simulation showed the steel tube assembly with air hole and solid steel rod distinguished clearly. GCTS program was also used for both 2D image reconstructions, 3D visualization of gamma transmission CT measurement and MCNP simulations.

5. Conclusion

The results of MCNP simulations gamma CT scan images showed clear resolution in identifying the overlying layer inside the PVC pipe column. MCNP Simulation studies presented valuable data to start the design and optimization of gamma CT scan imaging systems. MCNP simulations results also assist the modeling of experimental design and precise results for the confirmation of experimental work.

6. Acknowledgements

Current study was carried out under the Ph.D Research Program at the Department of Nuclear Physics, D.S.A. The authors gratefully thanks to head of department for allowing me to do this research work at Nuclear Physics Laboratory providing experimental facilities and all persons who contributed to accomplish every step of my research tasks regarding the development of automatic portable gamma computed tomography CT system.

7. References

- [1] Jongbum Kim, Sunghee Jung, Jinho Moon, Gyuseong Cho, "A feasibility study on gamma ray tomography by Monte Carlo simulation for development of portable tomographic system", Applied Radiation and Isotopes, www.elsevier.com Vol(7), pp 404-414, 2012.

- [2] Avinash C. Kak, Malcolm Slaney, “Principles of Computerized Tomographic Imaging”, IEEE PRESS, 1999.
- [3] Jongbum Kim, Sunghee Jung, Jinho Moon, and Gyuseong Cho, “Industrial gamma-ray tomographic scan method for large scale industrial plants,” Nuclear Instruments and Methods in Physics Research A, vol. 640 , pp. 139–150, 2011.
- [4] Patrick Marchand and O. Thomas Holland, “Graphic and GUIs with MATLAB”, third edition, The Mathworks Inc.,USA, 2003.
- [5]“An MCNP Primer”, J. K. Shultis and R. E. Faw, Kansas State University, Manhattan, 2004.